Ore Geology Reviews 146 (2022) 104949

Contents lists available at ScienceDirect

Ore Geology Reviews

journal homepage: www.elsevier.com/locate/oregeorev

Formation of the Banxi Sb deposit in Eastern Yangtze Block: Evidence from individual fluid inclusion analyses, trace element chemistry, and He-Ar-S isotopes

Shanling Fu [a,*], Tianxing Wang [a,b], Jun Yan [a], Lichuan Pan [a], Luming Wei [a,b], Qing Lan [a], Shengyun Fu [c]

[a] State Key Laboratory of Ore Deposit Geochemistry, Institute of Geochemistry, Chinese Academy of Sciences, Guiyang 550081, China
[b] College of Resources and Environment, University of Chinese Academy of Sciences, Beijing 100049, China
[c] Hunan Institute of Geological Survey, Changsha 410116, China

ARTICLE INFO

Keywords:
Individual fluid inclusion
Trace element chemistry
He-Ar-S isotopes
Formation mechanism
Banxi Sb deposit

ABSTRACT

The Banxi Sb deposit (>100,000 t Sb metal with a grade of 0.02%–64.5% Sb (typically 15.3%–25.9% Sb) in the Eastern Yangtze Block is hosted in Neoproterozoic low-grade metamorphic clastic rocks of the Banxi Group. The deposit is characterized by vein-type Sb-only mineralization. Analyses of individual quartz-hosted fluid inclusions obtained by LA-ICP-MS identified Na as the most abundant cation (thousands to tens of thousands of ppm) in the ore-forming fluids of the Banxi Sb deposit, together with variable contents of K, Ca, Al, As, Fe and Sb (tens to thousands of ppm). Multiple chemical criteria, including high Na^+/K^+ (typically 3–15) and low Mn^{2+}/Na^+ (0.003–0.2) and Sr^{2+}/Na^+ (0.001–0.01) ratios of individual fluid inclusions, suggest that the fluids responsible for quartz and stibnite precipitation in the Banxi Sb deposit were likely dominated by basinal brines within low-grade metasedimentary rocks. Moreover, the extremely low $^3He/^4He$ ratios (0.001–0.048Ra) but relatively high $^3He/^{36}Ar$ (0.5×10^{-5}–5.8×10^{-4}) and $^{40}Ar/^{36}Ar$ ratios (323–1111 with an average of 737) of fluid inclusions trapped in ore-stage quartz further support a sedimentary origin of ore-forming fluids in this deposit. The positive and homogeneous sulfur isotopic values ($\delta^{34}S$ = 8.0–9.5‰) of stibnite and arsenopyrite are comparable to those of sulfides in Proterozoic metasedimentary rocks ($\delta^{34}S$ = 5.6–11.5‰), indicating these metasedimentary rocks may have served as the primary source of S for the Banxi Sb deposit. Combined with geological features and new trace element chemistry data for quartz and stibnite, we envisaged a new formation model for the Banxi Sb deposit that assumes that circulation of weakly alkaline basinal brines through faults under an extensional tectonic setting during the Early Cretaceous (~130 Ma), mobilization of Sb and S from the underlying and host metasedimentary rocks and ascent of ore- forming fluids along faults, and ultimately precipitation of Sb minerals in or around fault/fracture zones as a result of the decreasing pH of the ore-forming fluids as well as sulfidation during fluid-rock reaction.

1. Introduction

The Xiangzhong Sb-Au metallogenic province (XZMP; in central Hunan) is situated at the eastern part of the Yangtze Block (Fig. 1a) and hosts a set of world- class Sb deposits such as the Xikuangshan, Woxi, Zhazixi, Banxi, Fuzhuxi, and Gutaishan, and hundreds of other medium- to small-sized Sb deposits, making it the largest Sb province in the world (Hu et al., 2017; Fu et al., 2020a). Known Sb deposits in this region can be grouped into two host types, considering mineralization style, host rocks and spatial distribution. The first type is characterized by stibnite as the only ore mineral without a polymetallic contribution, and is mainly hosted in Devonian to Carboniferous sedimentary rocks occurring within the Xiangzhong basin. This type is best represented by the giant Xikuangshan Sb deposit and can thus be termed the Xikuangshan-type (XKS-type). The second type is best exemplified by the Woxi Sb-Au-W deposit (termed the WX-type) and is characterized by Sb-polymetallic mineralization where the ore minerals comprise stibnite, pyrite, native gold, scheelite and arsenopyrite. The WX-type Sb deposits are mainly

* Corresponding author.
E-mail address: fushanling@mail.gyig.ac.cn (S. Fu).

https://doi.org/10.1016/j.oregeorev.2022.104949
Received 13 December 2021; Received in revised form 11 April 2022; Accepted 19 May 2022
Available online 23 May 2022

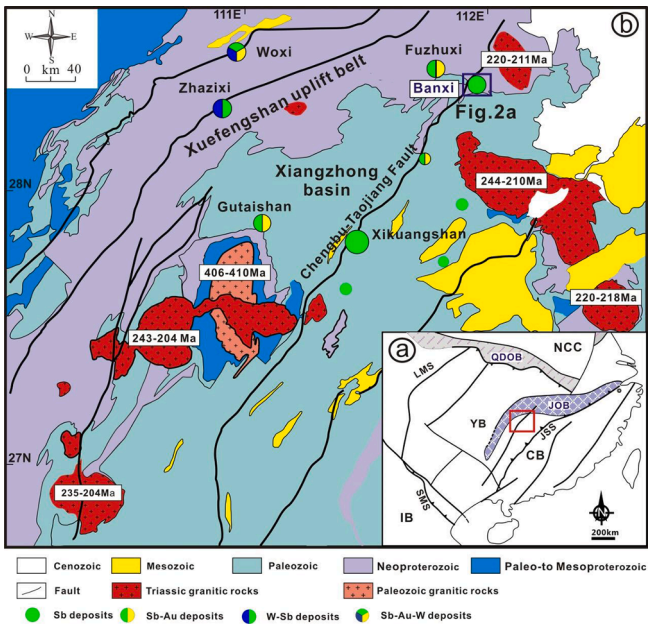

Fig. 1. a: Tectonic framework of South China Block showing the location of the Xiangzhong Sb-Au metallogenic province (Central Hunan) (modified from Qiu et al., 2016; Hu et al., 2017). **b:** Regional geological map of the Xiangzhong Sb-Au metallogenic province in the eastern part of the Yangtze Block showing the distribution of important Sb deposits (modified from HBGMR, 1988; Xie et al., 2019). Age data for granites are sourced from Wang et al. (2007a), Wang et al. (2012), Li et al. (2014), Fu et al. (2015) and Xie et al. (2019). CB- Cathaysia Block; IB-Indochina Block; JOB-Jiangnan Orogen Belt; JSS-Jiang-Shao Suture; LMS-Longmenshan Fault; NCC-North China Craton; QDOB-Qinling-Dabie Orogen Belt; SMS-Song-Ma Suture; YB- Yangtze Block.

hosted in Proterozoic low- grade metasedimentary rocks occurring in the Xuefengshan uplift belt (Fig. 1b; Hu et al., 2017; Li et al., 2018a, 2019a, b; Fu et al., 2020a, b).

Unlike the XKS-type and WX-type Sb deposits, however, the Banxi Sb deposit, situated within the transitional region from the Xuefengshan uplift belt to the Xiangzhong basin (Fig. 1b), was considered a transitional type between the aforementioned two types because it is hosted in Neoproterozoic low-grade metamorphic clastic rocks but features Sb-only mineralization (Li et al., 2018a; Fu et al., 2019). This deposit has been mined for more than a century with a total proven Sb metal reserve of approximately 100,000 tonnes and a grade of 0.02–64.5%Sb (mostly 15.3–25.9%; Hu et al., 2017; Li et al., 2020). However, the simple ore composition posed a challenge for clearly constraining the origin of the ore-forming fluids and the formation mechanism of this deposit, with some conceptual models favoring either a sedimentary, metamorphic, or magmatic origin based on geological observations and limited traditional isotope data (Li, 1996; Zhu et al., 2002; Wu and Chen, 2004; Tang et al., 2017; Li et al., 2018, 2019a,b). A remarkable feature of the Banxi Sb deposit is that stibnite is the only ore mineral and quartz is the predominant gangue mineral (Li et al., 2018, 2019a; Fu et al., 2019). Composition of individual fluid inclusions trapped in quartz by laser ablation–inductively coupled plasma-mass spectrometry (LA-ICP-MS) have been widely used to investigate the origin of ore-forming fluids and define the formation process of hydrothermal ore deposits (Heinrich et al., 1999; Audétat, 2019; Large et al., 2016; Shu et al., 2021). The trace element chemistry of cogenetic quartz and stibnite also could provide important and direct evidence for the fluid origin. In addition, He-Ar and S isotopes are useful in tracing the sources of ore-forming materials for hydrothermal ore deposits (Stuart et al., 1995; Burnard et al., 1999; Hu et al., 2004, 2012; Hoefs, 2015; Fu et al., 2020c). Therefore, a combination of individual fluid inclusion analyses, trace element chemistry of cogenetic quartz and stibnite and He-Ar-S isotopes of stibnite on the basis of field geological investigations will help to improve the understanding of the formation mechanism of the Banxi Sb deposit.

We conducted an integrated study of *in situ* quantitative determination of individual quartz-hosted fluid inclusions, trace element composition of major ore and gangue minerals and S isotopes of sulfide minerals, using Laser Ablation Inductively Coupled Plasma Mass Spectrometry (LA-ICP-MS) in addition to the analysis of He-Ar and S isotopes in hydrothermal sulfide minerals. The primary aim of this study is to characterize the origin of ore-forming fluids and to gain new insights into the formation mechanism of the Banxi Sb deposit.

2. Geological setting

2.1. Regional geology

The South China Block comprises the Yangtze Block to the northwest and the Cathaysian Block to the southeast (Fig. 1a), which were welded together along the Jiangshao suture during the Neoproterozoic period (Zhao et al., 2011; Hu and Zhou, 2012; Yao et al., 2016). The XZMP is located at the eastern part of the Yangtze Block and consists of the Xiangzhong basin and Xuefengshan uplift belt (Fig. 1b). The basement rocks of this region are composed of low-grade metamorphic rocks of Middle to Late Proterozoic and Early Paleozoic ages, and are mainly distributed in the Xuefengshan uplift belt and sub-uplifts within the Xiangzhong basin. Sedimentary rocks of Late Paleozoic to Mesozoic carbonate and clastic rocks mainly occur within the Xiangzhong basin (Fig. 1b; BGMRHN, 1988). Late Triassic granitic rocks (230–200 Ma), and, to a lesser extent, Early Devonian granitoids (410–400 Ma) intruded along the margin of the Xiangzhong basin (Fig. 1b), and were interpreted to have been produced by partial melting of Proterozoic metasedimentary rocks (Wang et al., 2007; Chu et al., 2012a; Fu et al., 2015; Xie et al., 2019). During the Early Palaeozoic, the Caledonian orogeny produced ductile shearing, intense folding and granitic magmatism (Faure et al., 2009; Charvet et al., 2010; Xie et al., 2019). The Xiangzhong basin formed between these uplifts and sedimentation resumed on the Proterozoic metamorphosed clastic rocks, which were unconformably overlain by late Paleozoic and early Mesozoic carbonate and clastic rocks (Shi et al., 1993; Ma et al., 2002). The Indosinian orogeny was probably the most important tectonic event in this region which resulted in the formation of NE-striking structures, the emplacement of granitic plutons and the folding of the strata in the basin (Wang et al., 2007; Chu et al., 2012a, b; Fu et al., 2015; Fig. 1b). During the Jurassic to Cretaceous, the earlier structures were reactivated and reworked and the entire Xuefengshan belt was uplifted further during the Yanshanian orogeny (Li et al., 2013). However, igneous rocks of this period are exceptionally scarce although geophysical data suggest that some concealed granite intrusions may be present at depth (Li, 1996; Rao et al., 1999). There are mainly three episodes of mineralization in this region: the 430–380 Ma and 230–200 Ma episodes of Sb-Au-W mineralization in the Xuefengshan uplift belt, the 160–130 Ma episode of Sb mineralization in the Xiangzhong basin and the granite- related W deposits in the northeast of this basin (Hu et al., 1996; Peng et al., 2003a, b; Wang et al., 2012; Hu et al., 2016, 2017; Li et al., 2018a, b; Fu et al., 2019, 2020b; Xie et al., 2019; Zhang et al., 2019; Wang et al., 2020).

2.2. Geology of the Banxi Sb deposit

The Banxi Sb deposit is located at the southeastern margin of the Xuefengshan uplift belt, a transitional zone to the Xiangzhong basin (Fig. 1b). The deposit consists of two ore blocks: Jiangjiachong and Xiaogang, from south to north (Fig. 2a). The major geologic attributes of the Banxi deposit have been documented in previous literature (Luo, 1995; Tang et al., 2017; Li et al., 2018a, 2019a, b; Fu and Shen, 2020), and details of the most important features are summarized as follows.

The strata outcropping in the Banxi Sb deposit mainly consist of the

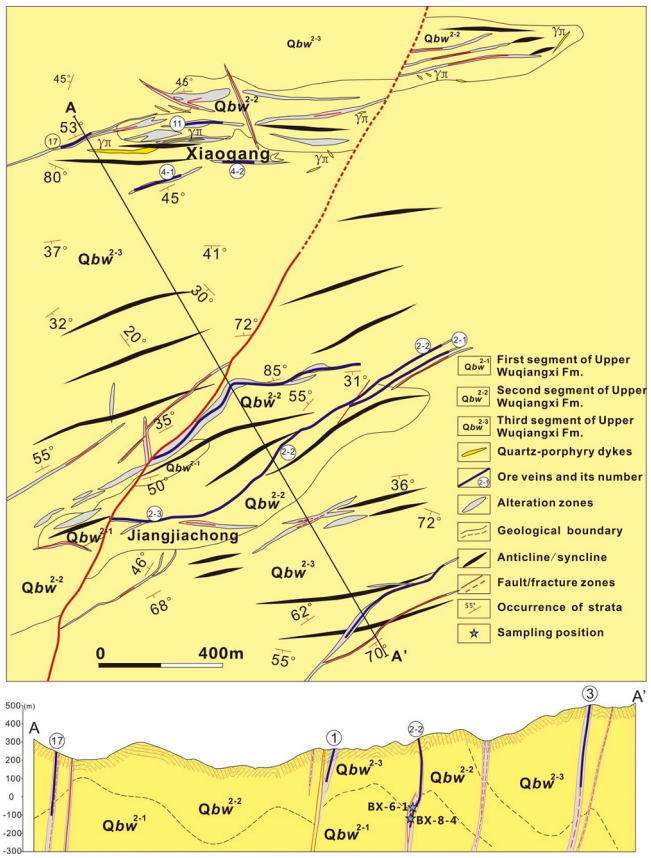

Fig. 2. a: Geological map of the Banxi Sb deposit and **b:** A-A' profile of the Banxi Sb deposit showing the shapes and distribution of ore veins in the Banxi deposit (modified after Fu and Shen, 2020).

Wuqiangxi Formation of the Banxi Group with a Neoproterozoic age, which contains regional low-grade metamorphic clastic rocks with original characteristics of a littoral facies-neritic facies flysch sedimentary sequence (BGMRHN, 1988). The Wuqiangxi Formation is conventionally further divided into three segments from bottom to top (Luo, 1995; Li et al., 2019a; Fu and Shen, 2020): (i) the first segment consists of grey-green metasedimentary tuff, tuffaceous siltstone, tuffaceous slate, sericite slate and sandy slate, locally interbedded with feldspathic quartz sandstone; (ii) the second segment consists of thick-bedded tuff, tuffaceous sericite slate and sericite slate; and (iii) the third segment comprises grey-black silty slate, purple slate, banded slate, sericite slate and silty sericite slate, which is locally interbedded with tuffaceous slate meta-tuff and meta-sandstone. Antimony mineralization at Banxi is mainly concentrated in the upper portion of the first segment and the bottom of the second segment (Luo, 1995; Fu et al., 2019; Fu and Shen, 2020).

Structurally, the Banxi deposit is chiefly defined by the NE-trending fault F_1 (part of the regional Taojiang-Chengbu fault) and its secondary ENE-trending faults, and a set of EW-trending complex folds including the Jiangjiachong and Xiaogang anticlines which controlled the distribution and occurrence of Sb mineralization (Luo, 1995; Fu and Shen, 2020; Fig. 2a). A set of ENE-trending secondary faults intersecting the main fault F_1 and extending along the axis of the Jiangjiachong and Xiaogang anticlines (Fig. 2a) was interpreted to have provided the conduit for ascending ore-forming fluids (Li et al., 2018a). Quartz-porphyry dikes in the northern part of the Banxi deposit (Fig. 2a) are major intrusion rocks with an U-Pb age of ~220 Ma, and are cut by quartz-stibnite veins and thus considered to be earlier than Sb mineralization (Zhao et al., 2005; Fu et al., 2019; Fu and Shen, 2020).

Orebodies of the Banxi deposit chiefly occur as veins. Six ore veins have been discovered in the Banxi deposit (Fig. 2a, b and Fig. 3) which are mainly hosted in the cores of anticlines and are strictly controlled by faults (Fig. 2b; Fu and Shen, 2020). The ore veins can be classified into two groups: (i) NE-trending veins including the V_1, V_2 and V_3 veins in the southern part of the Banxi deposit; and (ii) EW-trending veins, including V_4, V_{11} and V_{17}, which are mainly distributed in the northern part of the Banxi deposit. Among them, the V_2 ore belt is the largest and actively being mined. This ore belt occurs as an elongated "S" shape in plane view and has a length of over 2000 m along strike (Li et al., 2018a). It contains three separate veins from NE to SW (Fig. 2a), with thickness ranging from 0.3 to 2.1 m and a variable grade of 0.03% to 61.0% Sb. The mineral assemblage of the ores is relatively simple: stibnite is the principal ore mineral, with minor arsenopyrite; the gangue consists mainly of quartz, chlorite and sericite (Fig. 4). Three major stages were differentiated based on the cross-cutting relationship of ore veins and generation sequence of gangue- and ore-minerals, that is, the quartz, quartz-stibnite and stibnite stages (Li et al., 2018a), of which the quartz-stibnite stage has the majority of Sb reserves (Fu and Shen, 2020).

Fluid inclusion studies have suggested that the homogenization temperature of ore-forming fluids in the Banxi deposit ranges from 260 to 170 °C with the salinities of 3.4–7.7 wt% NaCl equiv. (Li et al., 2019a). The host rocks of Sb mineralization were intensively altered by ore-forming hydrothermal fluids (Fu and Shen, 2020; Li et al., 2020), which caused sericitization and silicification close to ore veins and chloritization further away from the ore veins (Li et al., 2020 and Fig. 5 therein).

Multiple methods have been employed to determine the precise age of Sb mineralization at Banxi. Peng et al. (2003a) proposed that Sb mineralization at Banxi may have taken place during Early Palaeozoic (397–422 Ma) by using quartz Ar-Ar dating. However, as stated above, the cross-cutting relationship between quartz- porphyry dykes and stibnite-quartz veins suggests that Sb mineralization at Banxi should occur later than 220 Ma. Most recently, the Rb-Sr and Sm-Nd dating results of hydrothermal sulfides and zircon (U-Th)/He dates reported by Li et al. (2018a, 2020) and Fu et al. (2019) have suggested the Banxi Sb deposit formed at ~ 130 Ma.

3. Samples and analytical methods

Because most ore veins of this deposit have been mined out or are not mining, all samples in this study were mainly collected from underground exposures of the V_2 ore belt in the Banxi deposit. One sample (BX-6-1), composed of coarse-grained stibnite and quartz veins, was taken from the sublevel #06 at an elevation of −60 m; one sample (BX-8-4) was taken from the sublevel #08 at an elevation of −120 m, which is composed of altered slate and fine-grained stibnite; two samples were taken from the sublevel #14 at an elevation of −375 m, of which the BX-14-2 is composed of fine-grained stibnite and quartz veins, and the BX-14-3 mainly consists of mainly coarse-grained stibnite; three samples were taken from the sublevel #15 at an elevation of −415 m, where the BX-15-1 is composed of quartz-stibnite veins, the BX-15-3 of pure stibnite, and the BX-15-3 of altered slate and fine-grained arsenopyrite; two samples were taken from the sublevel #19 at an elevation of −595 m, whereas the BX-19-1 is composed of coarse-grained stibnite and quartz veins, and the BX-19-2 comprises altered slate and coarse-grained arsenopyrite.

3.1. LA-ICP-MS analyses of individual fluid inclusions

Individual fluid inclusions trapped in quartz from the quartz-stibnite stage in the Banxi Sb deposit were analysed using an Agilent 7900 Quadrupole ICP-MS coupled with a NWR-193 UC laser ablation system at the Magmatic and Ore-Forming Processes Research Laboratory at the University of Toronto. An in-house trachytic glass standard doped with a broad range of trace elements was used for external standardization. The

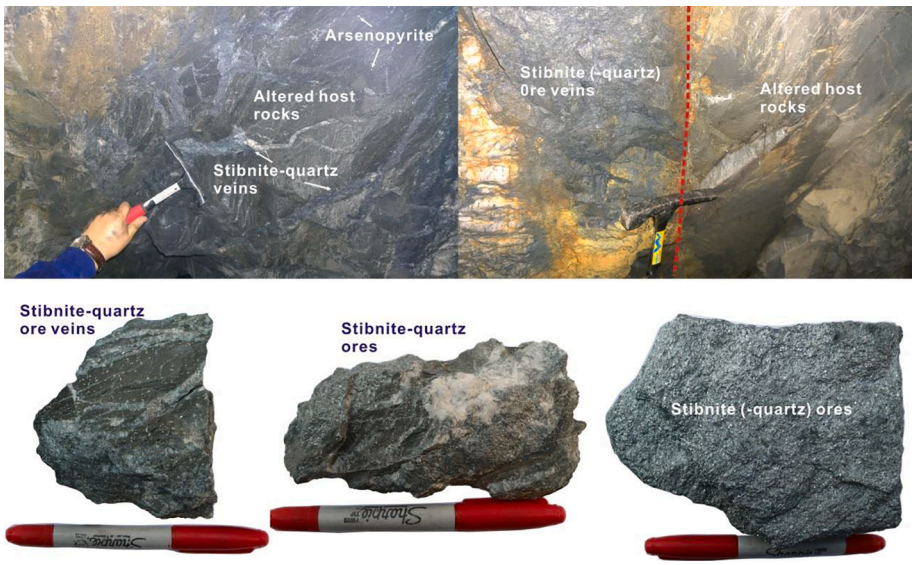

Fig. 3. Pictures of ore veins and hand specimen of various ores at the Banxi Sb deposit (The photo in the lower left is from Fu et al.(2019)).

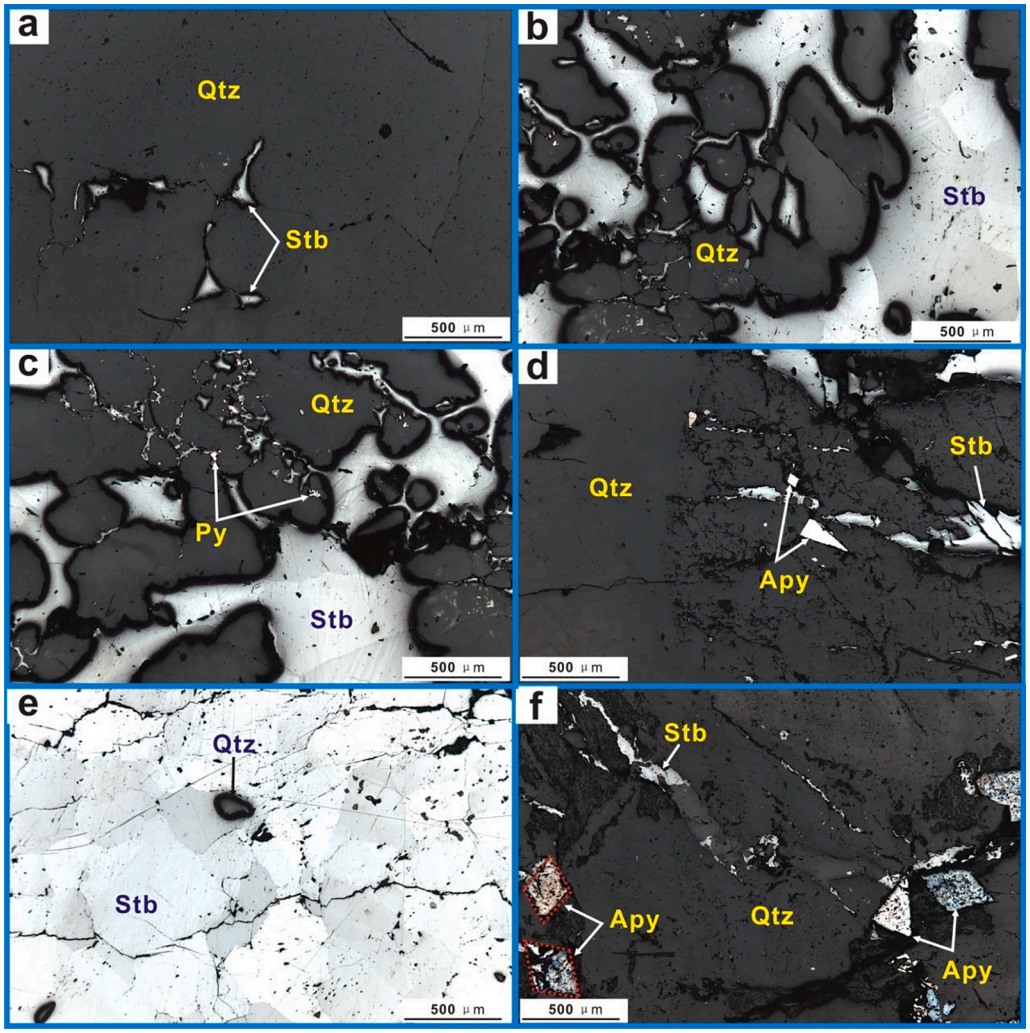

Fig. 4. Reflected light microphotographs of ores at the Banxi Sb deposit. (**a**). ore of quartz stage with weak Sb mineralization; (**b**)~(**d**) ores of stibnite-quartz stage; (**e**) and (**f**) ores of stibnite stage with minor quartz formed. Qtz-quartz, Stb- stibnite, Py-pyrite, Apy-arsenopyrite.

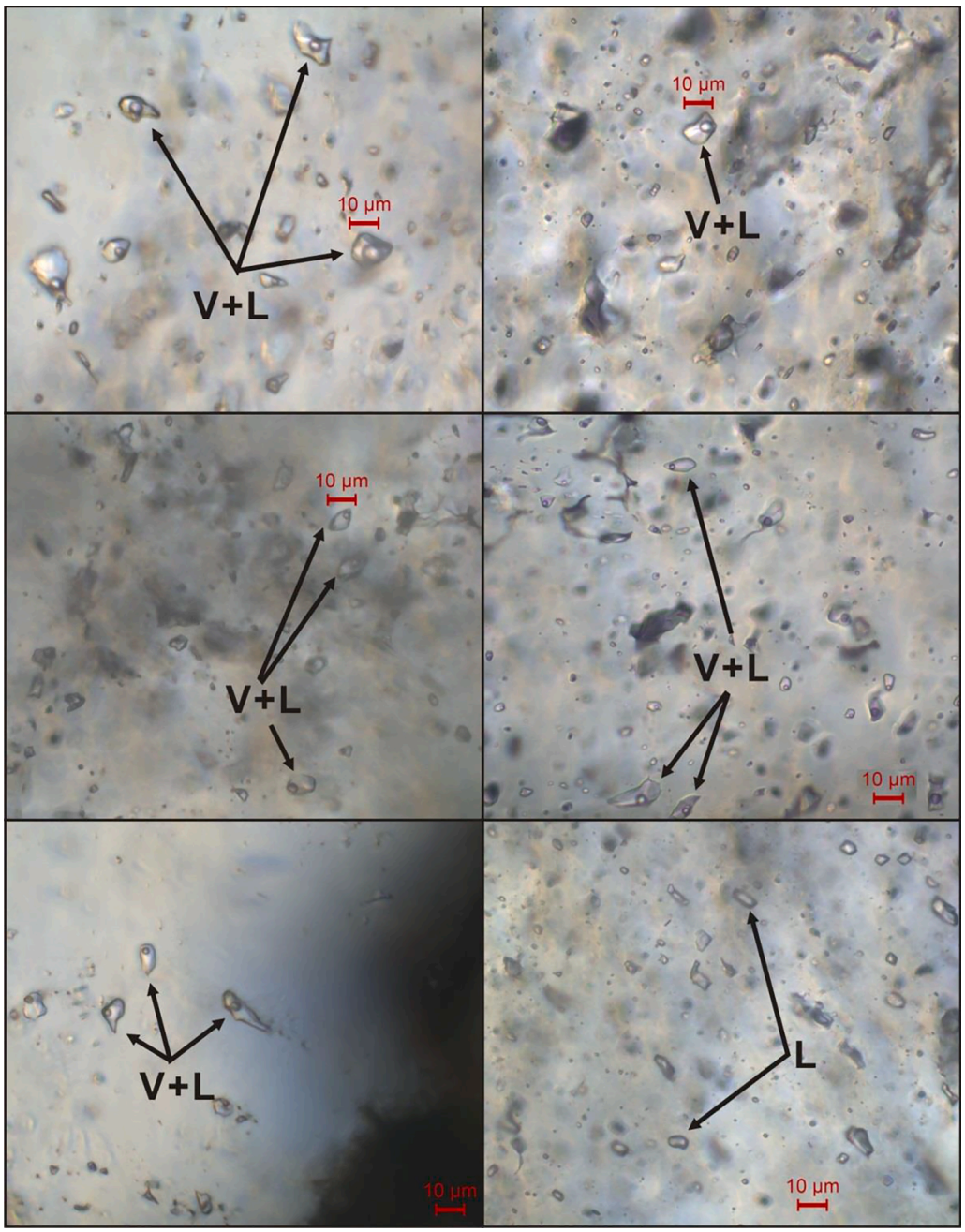

Fig. 5. Microphotographs of various types of fluid inclusions trapped in quartz at the Banxi Sb deposit. V + L-vapor-rich aqueous inclusions; L-liquid-rich inclusions.

carrier gas (He) flow of 1 l/min was used and the instrument was tuned to ThO/Th $\leq$ 0.3%, Mass 21/^{42}Ca $\leq$ 0.3%, and ^{238}U/^{232}Th of 1.0–1.1 using the NIST 610 glass. The laser beam diameter was adjusted for each analysis to ensure complete ablation of the fluid inclusion while minimising the blasting of the host quartz; thus, the spot diameter varied between 12 and 20 μm depending on the size of the fluid inclusions. Each analysis block consists of 12–15 fluid inclusion analyses bracketed by 2–2 external standard analyses at the beginning and the end. More details of the analytical method can be found in Yin and Zajacz (2018). A range of trace elements including B, Na, Mg, Al, Si, K, Ca, Ti, Mn, Fe, Cu, Zn, As, Rb, Sr, Mo, Ag, Sn, Sb, Cs, Ba, W, and Pb concentrations were measured in each fluid inclusion. Quantification of individual inclusion LA-ICP-MS signals involves the integration of each element, background subtraction, subtraction of host quartz contributions to the signal, and comparison of signal intensities with an external silicate glass standard (NIST 610). The ICP-MS yields only ratios, thus absolute elemental concentrations are derived by comparison of elemental ratios to independently derived estimates of wt. % NaCl equiv. from microthermometry. Trace element concentrations were corrected for the mass contribution of other major elements within the fluid inclusion (Halter et al., 2002; Heinrich et al., 2003). The raw LA-ICP -MS data were reduced using the SILLS program (Guillong et al., 2008), which has the capability to integrate multiple areas of the signal portions and gives concentrations of elements in both fluid inclusions and host quartz. The contribution of the host quartz to the mixed fluid-glass signals was removed assuming that all Si signals were from the quartz.

3.2. LA-ICP-MS trace element analyses

Quantitative determination of the trace element composition for stibnite from the quartz-stibnite and stibnite stages was conducted using an Agilent 7700x quadrupole ICP-MS coupled with a New Wave UP213

laser ablation system at the Institute of Geochemistry, Chinese Academy of Sciences (IGCAS). Laser ablation was conducted in a pure He atmosphere using an in-house small-volume sample cell and the aerosol was mixed with Ar as a transport gas immediately after leaving the cell. The measurement of spots was performed at laser pulse frequency of 10 Hz and spot size of 40 μm with laser energy of 3.5 J/cm^2. The analysis time for each spot was 120 s, comprising a 30-s measurement of the background with the laser off, and 60-s analysis with the laser on, and followed by a 30-s retention time to ensure proper cell washout. A linear drift correction based on the analysis sequence and on the bracketing analyses of MASS-1 was applied to the count rate for each sample. The dwell time was set to 10 ms for each element measured with a total sweep time of <0.5 s. External calibration was performed against the in-house standards (GSE-1G and GSD-1G), and sulfide reference material MASS-1 (formerly known as PSD-1; Wilson et al., 2002) was used as a secondary check (running as an "unknown") to monitor the analytical accuracy. The following isotopes were measured to avoid isobaric and polyatomic interferences: ^{7}Li, ^{27}Al, ^{29}Si, ^{34}S, ^{51}V, ^{53}Cr, ^{55}Mn, ^{57}Fe, ^{59}Co, ^{60}Ni, ^{65}Cu, ^{66}Zn, ^{71}Ga, ^{72}Ge, ^{75}As, ^{77}Se, ^{85}Rb, ^{88}Sr, ^{95}Mo, ^{105}Pd, ^{107}Ag, ^{111}Cd, ^{115}In, ^{118}Sn, ^{125}Te, ^{197}Au, ^{201}Hg, ^{205}Tl, ^{208}Pb, ^{209}Bi and ^{238}U. The raw analytical data in each spot are plotted as a time-resolved depth spectrum and the integration time for background and sample signal selected. The counts are then corrected for instrument drift and converted to concentration values using the Sb values as an internal standard. Synthetic standard glasses (NIST SRM 610 and 612) were additionally measured to recognize a possible instrumental drift. More details of the analytical processes and reduction of raw data could be found in Fu et al. (2020a).

The trace element composition of quartz from the quartz-stibnite stage was analyzed using an Agilent 7900 ICP-MS equipped with a GeoLasPro 193 nm ArF excimer laser at IGCAS, with conditions of a laser repetition of 10 Hz, energy density of 12 J/cm^2 and spot size of 44 μm. NIST SRM610 and GSD-1G were employed as external standard for quantitative calibrations, which was measured before and after each set of spots on a given sample. The analysis time for each spot was set at 90 s, comprising a 30-s measurement of the background with the laser off and a 60-s analysis with the laser on. An internal standard-independent calibration strategy was applied to the calibrations (Liu et al., 2008), which is based on the normalization of the sum of all metal oxides to 100 wt%. NIST SRM612 and GSD-1G were analyzed to monitor the accuracy of the results, which show that the uncertainties of most elements (e.g. Li, Na, Mg, Al, K, Ca, Sc, Ti, Sb, Ge, Rb and Sr) are <6% with detection limits ranging from few ppm to ppb. More details of the analytical procedures can be found in Lan et al. (2018).

3.3. He-Ar isotope analyses

He-Ar isotope analyses of stibnite and arsenopyrite were completed at IGCAS using an all-metal extraction line and a mass spectrometer (GV5400). The analytical methods are similar to those of Stuart et al. (1995), Hu et al. (2012) and Kendrick and Burnard (2013). However, more stibnite grains are required to extract sufficient He and Ar because of the low He-Ar abundance entrapped in stibnite. Approximately 1–5 g of separated coarse stibnite grains (generally 0.5–1.5 mm but the coarser the better) were ultrasonically cleaned in alcohol, dried, then loaded in on-line in vacuum crusher buckets. The samples were baked at 150 °C on-lined with the ultra-high vacuum system for >24 h prior to analysis in order to remove adhered atmospheric gases. Gases were released from the grains into the all-metal extraction system by sequential crushing in modified Nupro-type valves. The released gases were exposed to a titanium sponge furnace at 800 °C for 20 min to remove the bulk of active gases (e.g·H_2O and CO_2), and then exposed to two SAES Zr-Al getters (one at room temperature, the other at 450 °C) for 10 min for further purification. He was separated from Ar using an activated charcoal cold finger at liquid N_2 temperature (−196 °C) for 40–60 min to trap Ar. He and Ar isotopes and abundances were analyzed using GV5400. Gas abundances were measured by peak-height comparison with known amounts of standard air from an air bottle. He and Ar abundances and isotopic ratios were calibrated against pipettes of 0.1 cm^3 STP air (5.2×10^{-7} cm^3 STP ^{4}He and 9.3×10^{-4} cm^3 STP ^{40}Ar). Procedural blanks were $<2 \times 10^{-10}$ cm^3 STP ^{4}He and (2–4) $\times 10^{-10}$ cm^3 STP ^{40}Ar, and constituted <1% of analyses. The blank was too low to affect the calibration of the abundance measurement.

3.4. LA-ICP-MS S isotope analyses

The *in situ* analysis of S isotopic compositions of stibnites and arsenopyrite in ores was conducted by LA-MC-ICP-MS at the State Key Laboratory of Continental Dynamics, Northwest University, China. The laser ablation system (RESOlution M-50), consisting of an excimer laser (193 nm), a two-volume laser ablation cell (Laurin Technic S155), a Squid smoothing device, and a computer-controlled high- precision X-Y stage, was linked to MC-ICP-MS (Nu Plasma 1700) for *in situ* analysis of S isotope. The Nu 1700 MC-ICP-MS system equipped with sixteen Faraday cups and three ion counters was used to determine the sulfur isotopic composition of the PSPTs. The cup configurations for sulfur were as follows: an H5 cup for ^{34}S, an Ax cup for ^{33}S, and an L4 cup for ^{32}S. Helium was used as the carrier gas for the laser ablation process, and it entered the cell body at its bottom to fill the cell. Helium from both the bottom and top through the funnel cell entrained the sample aerosol and argon was admixed downstream, in front of the squid signal smoothing device, into the MC-ICP-MS. Instrumental bias was corrected using the SSB approach with repeated measurements of the standard reference (IAEA-S-1, Ag_2S), before and after each sample. For monitoring the accuracy of data during analysis, the in-house standard Cpy-1/GC ($\delta^{34}S = -0.7 \pm 0.3‰$) was analyzed every 8 spots. More details on the method are provided by Chen et al. (2017) and Yuan et al. (2018).

4. Results

4.1. Chemical composition of individual fluid inclusions

Microanalyses using LA-ICP-MS were performed on 124 individual inclusions. Relatively large inclusions (>10 μm; Fig. 5) were targeted because of the lower detection limits due to larger amounts of liquid. Because vapor-rich and vapor-only inclusions contained insignificant amounts of liquid phase, no apparent transient signal could be identified. Accordingly, in this case we report only values from liquid-rich inclusions, and the Electronic Supplementary Table S1 details the composition of individual fluid inclusions. These inclusions contain elevated concentrations of Na (2,943–19,489 ppm), Ca (2, 431–14,237 ppm), K (956–8,274 ppm), Al (137–24,782 ppm), Fe (324–12,349 ppm), and Sb (>23–7,957 ppm) and commonly contain measurable concentrations of B, As, Mg, Zn, Mn, Ti, Cu, Ba, Sr, Ag, Cs, W and Rb (typically < 100 ppm; Fig. 6a). Other elements (e.g., Au, Sb, Bi and Mo) are typically at or less than detectable quantities.

4.2. Trace element composition of stibnite and quartz

Forty-one spot analyses are conducted on five hydrothermal quartz samples collected from different sublevels. Trace elements with elevated concentrations routinely above the limits of detection are summarized in Fig. 6b and the full dataset of trace element composition of investigated quartz is presented in the Electronic Supplementary Table S2. Aluminum, Sb, Li, Na, K, Ge, B, Mg, Sc, Ti, and As are the most common trace elements, with concentrations of typically > 1–10 ppm (Fig. 6b); concentrations of other elements (V, Fe, Mn, Co, Ga, Cu, Zn, Rb, Ag, Pb, Se, Te, In, Cd, Sn, Au, and Bi) are typically at or below the limit of detection (generally lower than 1 ppm). Notably, the concentrations of major measured trace elements in quartz from the Banxi Sb deposit are relatively lower than those in the XKS-type and WX-type Sb deposits. For example, the Al and Sb concentrations in quartz are generally one to two

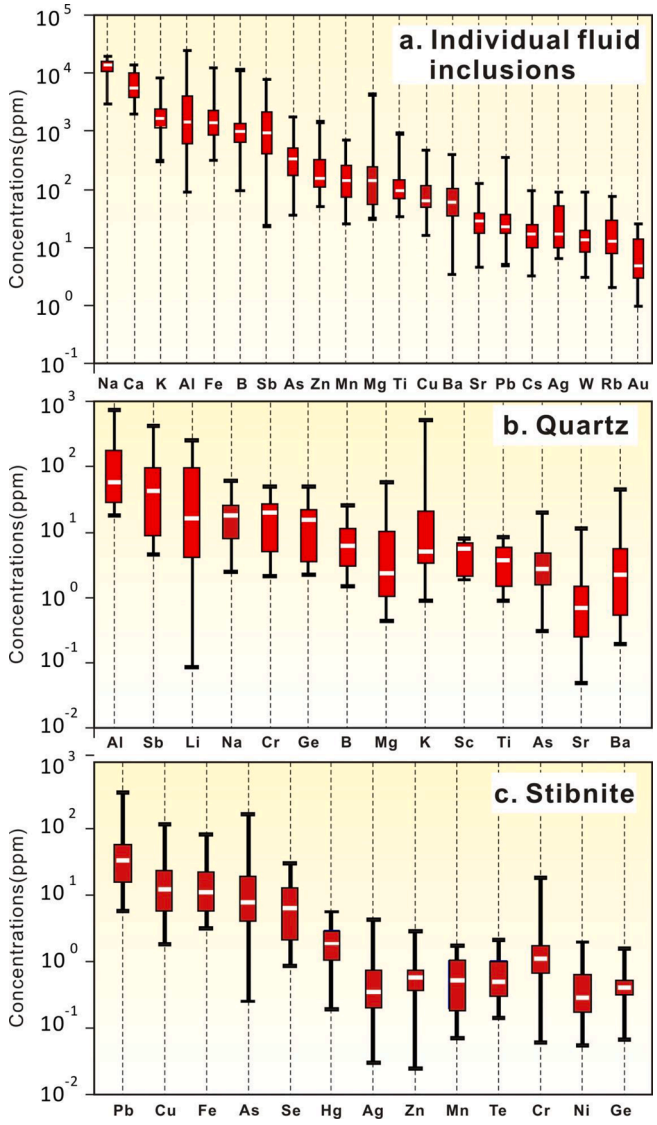

Fig. 6. Box diagrams of trace element compositions for (**a**) individual fluid inclusions trapped in quartz, (**b**) quartz, and (**c**) stibnite at the Banxi Sb deposit.

orders of magnitude lower than those from the Xikuangshan Sb deposits (generally > 1000 ppm; Fu et al., 2020c).

Likewisely, sixty spot analyses of trace elements were acquired on ten stibnite samples. Because many elements were detected at extremely low concentrations or below detection limits, elements with elevated concentrations well above the detection limits are included in Fig. 6c and the full dataset trace element composition of the investigated stibnite samples are given in the Electronic Supplementary Table S3. Because only a few elements can be incorporated into stibnite, Cu, Pb, As and Fe are the most abundant trace elements which may be present in the form of nanoparticles or micro-inclusions in stibnite, with concentrations of typically < 100 ppm (Fig. 6c). Despite our efforts to avoid visible inclusions, some analyses showed anomalous concentrations which might be a result of the presence of mineral or fluid inclusions. For example, the high variability of the As concentration (Fig. 6c) probably indicates the presence of As-rich inclusions in stibnite.

4.3. He-Ar isotopes of stibnite and arsenopyrite

The abundances and isotopic compositions of He and Ar in fluids trapped in stibnite and arsenopyrite from the Banxi Sb deposit are illustrated in Table 1 and Fig. 7. The concentrations of ^{4}He and ^{40}Ar range from 3.81×10^{-7} to 49.13×10^{-7} cm^3 STP/g and 0.43×10^{-7} to 19.00×10^{-7} cm^3 STP/g, respectively. The $^{40}Ar/^{36}Ar$ ratios vary from 323 to 1111, with an average value of 737, which is much higher than the atmospheric value of 296.2 (Mark et al., 2011). The $^{3}He/^{4}He$ ratios for stibnite and arsenopyrite were extremely low varying from 0.001 to 0.048 Ra. Notably, the $^{3}He/^{4}He$ ratios for stibnite are slightly higher than those for arsenopyrite (Table 1).

4.4. Sulfur isotopic composition of stibnite and arsenopyrite

Twenty-three LA-ICP-MS sulfur isotope analyses are conducted on eighteen stibnite grains and five arsenopyrite grains, and the results are shown in Table 2 and Fig. 8. The stibnite and arsenopyrite grains from the Banxi Sb deposit possess relatively positive and homogeneous sulfur isotopic compositions. The $\delta^{34}S$ values of stibnite grains range from $+8.0 \pm 0.19‰$ to $+9.5 \pm 0.32‰$ with an average of $+8.64 \pm 0.19‰$; the $\delta^{34}S$ values of arsenopyrite grains vary from $+7.9 \pm 0.28‰$ to $+8.9 \pm 0.19‰$ with an average of $8.73 \pm 0.46‰$.

Table 1
He-Ar isotopic composition of stibnite and arsenopyrite from the Banxi Sb deposit.

Sample No.	Mineral	Location	Weight	^{4}He ($10^{-7}cm^3STP$)/g	^{40}Ar ($10^{-7}cm^3STP$)/g	$^{3}He/^{4}He$ (Ra)	δ	$^{40}Ar/^{36}Ar$	δ	$^{40}Ar^*/^{4}He$	$^{3}He/Q$ (10^{-15} cm^3 STP J^{-1})
BX-6-1	Stibnite	Sublevel #06	0.51	3.81	19.00	0.025	0.003	1111.04	12.30	3.648	0.174
BX-6-2	Arsenopyrite	Sublevel #06	0.44	27.98	0.464	0.001	0.000	750.29	8.54	0.010	52.468
BX-8-4	Arsenopyrite	Sublevel #08	0.48	28.19	0.883	0.009	0.001	1106.17	13.34	0.023	27.736
BX-14-2	Arsenopyrite	Sublevel #14	0.41	23.47	0.431	0.009	0.002	864.21	11.37	0.012	47.335
BX-15-3	Stibnite	Sublevel #15	0.38	49.13	7.29	0.048	0.006	323.35	3.56	0.012	5.856
BX-15-5	Arsenopyrite	Sublevel #15	0.32	20.90	0.53	0.017	0.001	596.44	7.02	0.013	34.407
BX-19-2	Arsenopyrite	Sublevel #19	0.41	19.34	1.12	0.007	0.001	408.90	4.59	0.016	14.960

Notes: $^{40}Ar^*$ is non-atmospheric Ar, $^{40}Ar^*=^{40}Ar-[^{36}Ar \times 298.6]$; The $^{3}He/Q$ was calculated using the equation $^{3}He/Q = {}^{3}He/^{36}Ar \times [^{36}Ar]_{masw}/(Cp\theta)$, where $[^{36}Ar]masw$ is the concentration of ^{36}Ar in modified air saturated water, Cp is the specific heat of MASW and θ is the temperature increase of the cold fluid (°C) (Burnard and Polya, 2004).

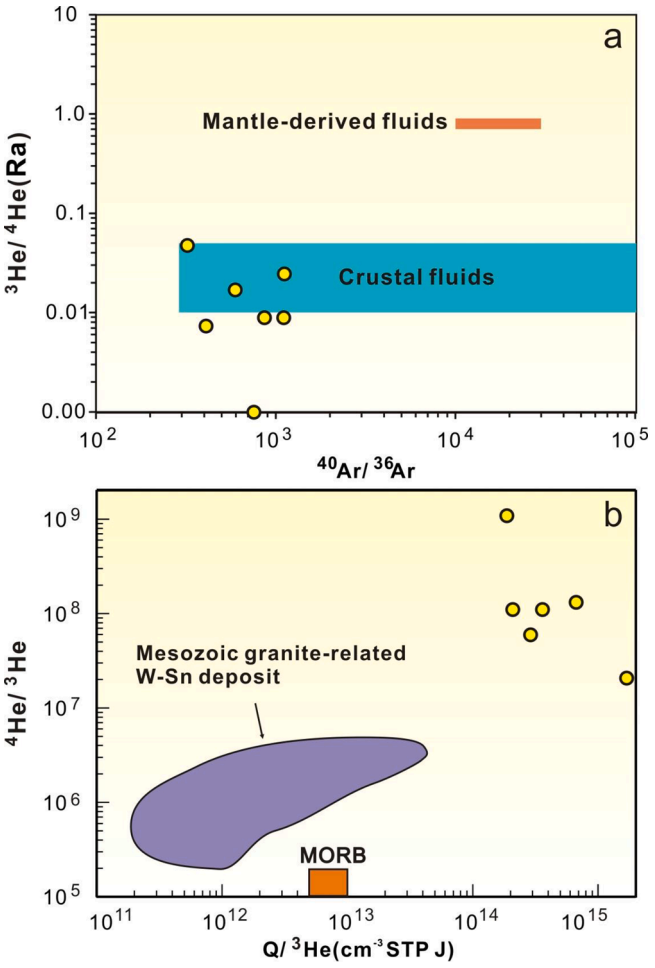

Fig. 7. a: Plot of ^{40}Ar/ ^{36}Ar vs ^{3}He/^{4}He of fluid inclusions trapped in arsenopyrite and stibnite from the Banxi Sb deposit, where the ranges of mantle and crustal fluids are defined by the data from Turner et al. (1993), Stuart et al. (1995), Burnard et al. (1999) and Hu et al. (2012). **b:** Plot of Q/^{3}He vs ^{4}He/^{3}He of the fluid inclusions trapped in sulfide minerals from the Banxi Sb deposit (modified after Burnard and Polya, 2004), where the range of the Mesozoic granite-related W-Sn deposits is calculated using the data from Hu et al. (2009; 2012), Wu et al. (2011, 2018), and Wei et al. (2019).

5. Discussion

5.1. Origin of ore-forming fluids

The origin of the hydrothermal fluids from which the Banxi deposit formed has long been a matter of debate and previous studies have suggested that the fluids were of sedimentary, metamorphic, or magmatic origin based on traditional fluid-inclusion and equivocal stable isotope data (Li, 1996; Zhu et al., 2002; Wu and Chen, 2004; Li et al., 2018, 2019a, b). Notably, because the latest metamorphic event documented in the studied region (460–400 Ma; Faure et al., 2009; Li et al., 2010; Wan et al., 2010) occurred approximately 300 million years ago before the timing of Sb mineralization (~130 Ma; Li et al., 2018a; Fu et al., 2019) at Banxi. Many studies have demonstrated that low-grade metamorphism (e.g., subgreenschist face) cannot cause significant mobility of Sb from sedimentary protoliths (Pitcairn et al., 2006, 2015; Phillips and Powell, 2010; Garofalo, 2012). Therefore, the typical metamorphic fluids are unlikely to be primary components of the fluids for forming the Banxi Sb deposit. Contrastingly, our new data favor the dominance of basinal brines in the ore-forming fluids of the Banxi Sb deposit with the addition of meteoric water.

Multiple criteria based on element concentrations and ratios measured by LA- ICP-MS analysis can be used to trace fluid sources. For example, the Na^+/K^+ ratio (molar ratio) of a series of fluid inclusions is generally used to discriminate fluid sources (Lu et al., 2004; Rusk et al., 2004; Simpson et al., 2015; Pan et al., 2019). Magmatic-derived hydrothermal fluids have a Na^+/K^+ ratio of <1, fluids derived from a sedimentary source (e.g. basin brines) at depth have a higher Na^+/K^+ ratio (e.g., ~17 for MVT Pb-Zn deposits; Lu et al., 2004; Pan et al., 2019; Zou et al., 2020). The Na^+/K^+ ratios of most fluid inclusions from the Banxi deposit range from 3 to 20, which are higher than those of magmatic but are comparable to the values for basinal brines in sedimentary rocks. Moreover, the source of fluids can be inferred from their trace element compositions (Large et al., 2016). In general, hydrothermal fluids derived from a magmatic source are generally enriched in

Table 2
In-situ sulfur isotopic composition of stibnite and arsenopyrite from the Banxi Sb deposit.

Sample No.	Mineral	Location	$\delta^{34}S_{V\text{-}CDT}$(‰)	2δ(‰)
BX-6-1-01	Stibnite	Sublevel #06	8.5	0.12
BX-6-1-02	Stibnite	Sublevel #06	8.5	0.14
BX-6-1-03	Stibnite	Sublevel #06	8.6	0.11
BX-6-1-04	Stibnite	Sublevel #06	8.4	0.13
BX-6-1-05	Stibnite	Sublevel #06	8.4	0.12
BX-6-1-06	Stibnite	Sublevel #06	8.3	0.10
BX-8-6-01	Stibnite	Sublevel #08	8.0	0.19
BX-14-2-01	Arsenopyrite	Sublevel #14	8.8	0.29
BX-14-2-02	Stibnite	Sublevel #14	8.4	0.12
BX-14-2-03	Arsenopyrite	Sublevel #14	8.8	0.24
BX-14-5-01	Stibnite	Sublevel #14	9.1	0.27
BX-14-5-02	Arsenopyrite	Sublevel #14	8.7	0.26
BX-14-5-03	Stibnite	Sublevel #14	9.2	0.14
BX-14-5-04	Stibnite	Sublevel #14	8.8	0.14
BX-15-1-01	Stibnite	Sublevel #15	8.3	0.13
BX-15-1-02	Arsenopyrite	Sublevel #15	7.9	0.28
BX-15-3-01	Stibnite	Sublevel #15	9.4	0.13
BX-15-3-02	Stibnite	Sublevel #15	9.1	0.13
BX-19-1-01	Stibnite	Sublevel #19	9.5	0.32
BX-19-1-02	Arsenopyrite	Sublevel #19	8.9	0.15
BX-19-1-03	Stibnite	Sublevel #19	8.5	0.13
BX-19-1-04	Stibnite	Sublevel #19	8.7	0.12

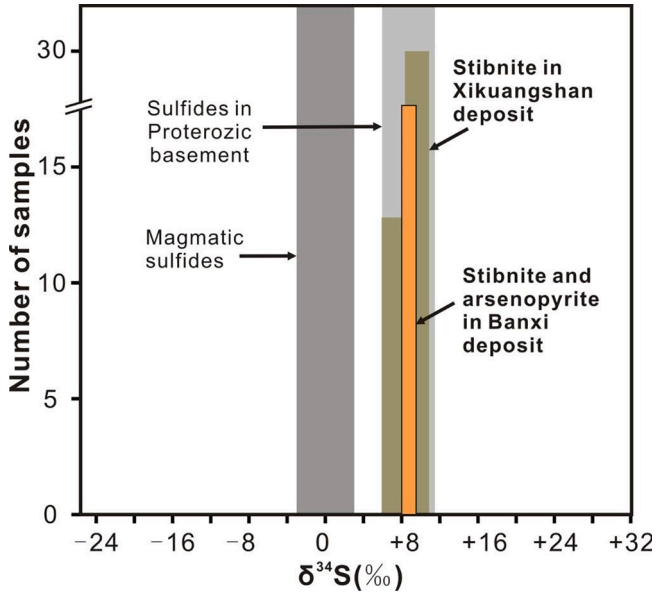

Fig. 8. Sulfur isotopic composition of sulfide minerals from the Banxi Sb deposit and potential source rocks. Data sources: magmatic sulfides from Chaussidon et al. (1989); sulfides in basement metamorphic rocks: Jiang et al. (1990), Ma et al. (2003), and Gu et al. (2012); stibnite in the Xikuangshan from Fu et al. (2020c).

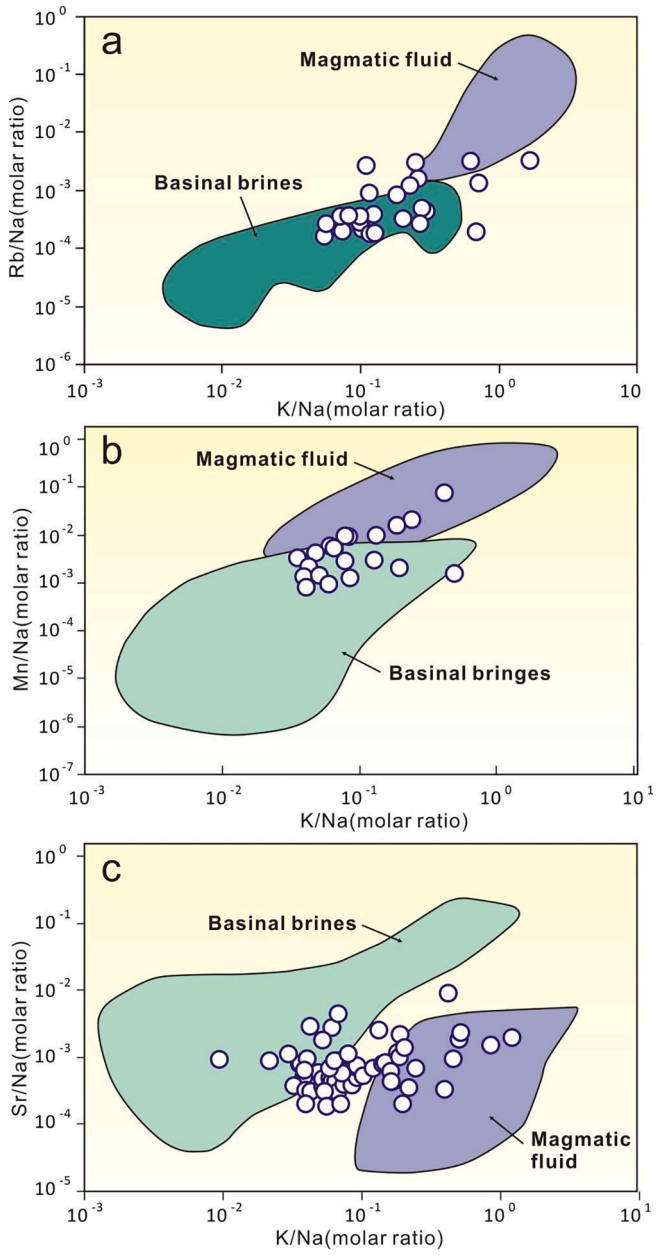

Fig. 9. Plots of (a) K/Na vs Rb/Na, (b) K/Na vs Mn/Na and (c) K/Na vs Sr/Na molar ratios of the fluid inclusions entrapped in quartz at the Banxi Sb deposit. The ranges for magmatic fluid, basinal brine, and sedimentary fluids are defined by data from Heijlen et al. (2008), Samson et al. (2008), Williams-Jones et al. (2010), Shu et al. (2017, 2021) and references therein.

alkali metals (Li, K, Rb, and Cs), whereas basinal brines tend to be enriched in alkaline earth elements (Ca, Sr, and Mg) (Samson et al., 2008; Williams-Jones et al., 2010; Kharaka and Hanor, 2014; Shu et al., 2021). The fluid inclusion data obtained in this study are plotted in the Rb/Na vs K/Na and Mn vs Na diagrams (Fig. 9a, b), most of which fall outside the characteristic areas of magmatic- hydrothermal fluids but are close to those of basinal brines acquired from Samson et al. (2008) and Williams-Jones et al. (2010). The elevated B contents (typically > 500 ppm) and low Mn/Na and Sr/Na ratios of most fluid inclusions in fluid inclusions also support the dominance of basinal brines in ore-forming fluids (Fig. 9b–d; Kharaka and Hanor, 2014). Additionally, the Cs/Rb ratios are generally applied to identify the diversity of fluid sources because Cs and Rb are considered to be largely conservative fluid components during hydrothermal processes (Klemm et al., 2008; Korges et al., 2018). The measured Cs/Rb ratios for the fluids in the Banxi range within a limited range (0.22–3.69), indicating that the fluids of different stages evolved from a similar fluid source without significant dilution by an external fluid source during quartz precipitation. A positive correlation was identified between the Cs and Rb contents in fluid inclusions, further indicating that ore-forming fluids for different stages in this deposit share a common source. It is thus reasonable to suppose that ore-forming fluids of the Banxi Sb deposit are probably dominated by basinal brines, which would be further supported by following He-Ar isotopic data.

Sulfide minerals, including stibnite and aresenopyrite, have been proven a faithful trap of noble gases in parental fluids (Stuart et al., 1994; Baptiste and Fouquet, 1996; Burnard et al., 1999; Hu et al., 1999). He-Ar isotopes in hydrothermal sulfides have been widely used for tracing the source of ore-forming fluids because a factor of ~1000 times difference between $^{3}He/^{4}He$ ratios of the upper mantle (6–9Ra, where Ra is the atmospheric $^{3}He/^{4}He$ ratio, 1.39×10^{-6}) and He produced in the crust (<0.05 Ra) allows He isotopes to provide an unique insight into processes where mantle volatiles have been added to crustal fluids (Stuart et al., 1995; Burnard et al., 1999; Burnard and Polya, 2004; Hu et al., 2004, 2009, 2012; Wu et al., 2018). Helium and Ar in fluid inclusions trapped in hydrothermal minerals are generally derived from the air- saturated water (ASW), mantle-derived volatiles and radiogenic decay of U, Th and K in crustal rocks with distinct He-Ar isotope ratios (Stuart et al., 1995; Burnard et al., 1999). The stibnite and arsenopyrite separates, recovered from underground samples at Banxi, are euhedral crystals with no evidence of post-crystallization modification; therefore, the measured He and Ar isotopes of the volatiles extracted from the stibnite and aresenopyrite separates at the Banxi Sb deposit can be used to represent the initial isotope compositions of the ore-forming fluids.

The $^{3}He/^{4}He$ ratios in fluid inclusions determined in this study range from 0.001 to 0.048 Ra and are much lower than the upper mantle value of 6–9 Ra but are close to the value for the fluids with a crustal origin (typically < 0.1 Ra, ranging from 0.05 to 0.1 Ra; Stuart et al., 1995; Fig. 7a), indicating a crustal origin of He in the fluids at Banxi. The $^{3}He/^{36}Ar$ ratios of 0.5×10^{-5}–5.81×10^{-4} measured in the study are much higher than those of ASW and the atmosphere (5×10^{-8} and 2×10^{-7}, respectively; Stuart et al., 1995), and the $^{40}Ar/^{36}Ar$ ratios (323 to 1111 with an average of 737) of the fluids for the Banxi Sb deposit is significantly higher than the atmospheric value of 296.2 (Mark et al., 2011), indicating that the fluids for the Banxi deposit were unlikely generated dominantly from meteoric water. Furthermore, if the magmatic heat flux is injected into the fluid it would have a high He/heat ratio ($^{3}He/Q$) otherwise it would have low $^{3}He/Q$ values (Castro et al., 2005, 2007). The $^{3}He/Q$ ratio can be obtained through the equation $^{3}He/Q = {}^{3}He/{}^{36}Ar \times [{}^{36}Ar]_{masw}/(C_p\theta)$, in which $[{}^{36}Ar]_{masw}$ is the concentration of ^{36}Ar in modified air saturated water (MASW), Cp is the specific heat of MASW, and θ is the temperature increase in the cold fluid (Burnard and Polya, 2004). The estimated $^{3}He/Q$ ratios of the fluids from the Banxi Sb deposit range from 0.17×10^{-15} to 52.47×10^{-15} cm^3 STP J^{-1} (Table 1), which are two to three orders of magnitude lower than those recorded by the hydrothermal fluids of the mid-oceanic ridge vents ($0.1–1.0 \times 10^{-12}$ cm^3 STP J^{-1}) (Lupton et al., 1989; Baker and Lupton, 1990), and the coeval granite-related W-Sn polymetallic deposits (Fig. 7b) to the east of this deposit, indicating that magmatic-origin fluids may contribute little to ore-forming fluids in the Banxi Sb deposit. The aforementioned evidence suggests that the ore-forming fluids for the Banxi Sb deposit may be dominated by basinal brines. Notably, the relatively low salinity of ore-forming fluids at Banxi compared with that of basinal brines implies minor input of low-salinity water of possible meteoric origin during stibnite precipitation.

5.2. Sources of sulfur in ore-forming fluids

Sulfur isotopes can provide insights into the origins of sulfide minerals and the ore-forming temperatures (Ohmoto and Rye, 1979; Hoefs,

2015). Considering the simple mineral association of stibnite-dominated and absence of sulfate minerals in the Banxi Sb deposit, the $\delta^{34}S$ values of stibnite can approximately represent that of the total sulfur in ore-forming fluids of this deposit (Seal, 2006). In contrast with prior results using bulk analysis methods ($\delta^{34}S = 1.1–6.7‰$; Luo, 1994; Li et al., 2019a), the $\delta^{34}S$ values of stibnite at Banxi acquired by LA-ICP-MS in this study were higher and clustered in a narrow range of 8.0–9.5 ‰, indicating that the sulfur in ore-forming fluids for different mineralization stages in the Banxi Sb deposit had a common origin or was derived from the same source region. These values are higher than those of magmatic sulfur (0 ± 5‰; Ohmoto, 1986) and the stibnite from the adjacent Woxi deposit (−2.8‰ to −2‰; Gu et al., 2012), but are close to those from the Xikuangshan Sb deposit (+6.8‰ to +10.2‰; Fu et al., 2020c) as well as the mean $\delta^{34}S$ values of sulfides in the Proterozoic basement rocks (+5.6‰ to +11.5‰; Fig. 8; Jiang et al., 1990; Ma et al., 2003; Gu et al., 2012). Analogously, these basement rocks are also most probably the Sb source for Sb deposits in South China (Fu et al., 2020c; Hu, 2021; Zhai et al., 2021) as these rocks contain the highest Sb abundance in the studied region (7.8–27.2 ppm; Lu et al., 2001; Ma et al., 2002). In addition, hydrothermal leaching experiments indicate that 20–90% of Sb can be transferred from this type of rocks to the fluids at 200 °C (Niu and Ma, 1991; He and Ma, 1996; Ma et al., 2002), further supporting the Proterozoic basement rocks may have served as the primary source of Sb for the Banxi deposit. Therefore, it is reasonable to speculate that the Proterozoic ore-host rocks or/and underlying basement sequences may account for the primary sulfur and Sb source of ore-forming fluids for the Banxi Sb deposits.

5.3. Transportation and precipitation mechanism of Sb

Antimony in natural hydrothermal solutions can be transported in the form of sulfide, hydroxide and chloride complexes, and are primarily controlled by temperatures and pH of hydrothermal systems (Krupp, 1988; Spycher and Reed, 1989; Wood et al., 1987; Oelkers et al., 1998; Zotov et al., 2003; Pokrovski et al., 2006). For example, the sulfide species (e.g., $Sb_2S_4^{2-}$, $HSb_2S_4^-$) dominate at low temperatures (<200–250 °C) S-rich solutions of neutral-to-alkaline pH (Williams-Jones and Normand, 1997; Zotov et al., 2003 and references therein). Neutral hydroxide species (e.g., $Sb(OH)_3$) are responsible for the transportation of Sb at temperatures greater than 200–250 °C over a wide range of pH. In the case of the Banxi Sb deposit, the pH value of ore-forming fluids was estimated at 5.59, based on fluid inclusion microthermometry data (Li et al., 2019a), indicating that the Sb in ore-forming fluids of this deposit might be not complexed with chlorine and sulphur ligands but more likely transported as the stable neutral hydroxyl complexes. A poor correlation between Na and Sb contents

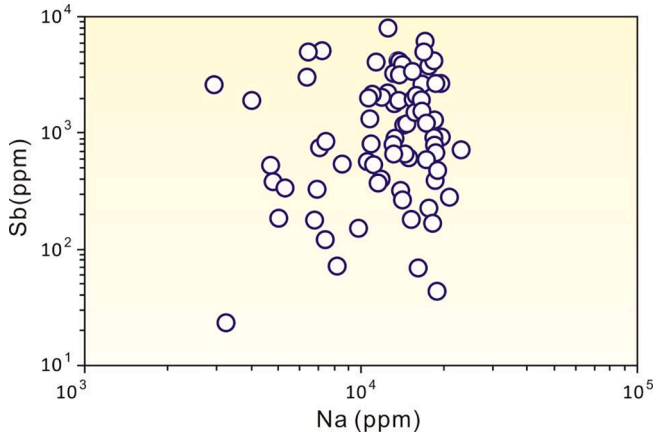

Fig. 10. Plot of Na vs Sb contents of fluid inclusions trapped in quartz at the Banxi Sb deposit.

(Fig. 10) in fluid inclusions trapped in ore-stage quartz from the Banxi Sb deposit further suggests that Sb is probably transported as neutral hydroxyl complexes of $Sb(OH)_3$. Previous experiments have demonstrated that Sb can be transported in the form of neutral hydroxyl complexes $Sb(OH)_3$ in hydrothermal environments over a wide range of temperatures (Pokrovski et al., 2002; Zotov et al., 2003).

Previous studies have suggested that the solubility of stibnite in hydrothermal fluids is generally dependent on temperature, pH and sulfur fugacity (Williams-Jones and Normand, 1997; Pokrovski et al., 2002; Obolensky et al., 2007). For example, the solubility of stibnite in hydrothermal solutions is as low as 0.1 ppm at pH conditions below neutrality (pH < 5.6) and stibnite dissolves independently of pH and fO_2 while, its solubility increases to 4.6 ppm Sb at higher pH (Williams-Jones and Normand, 1997). The measured Sb concentrations in fluid inclusions at the Banxi Sb deposit (generally > 1000 ppm; Fig. 6c) are much higher than the modelled Sb solubility in the acid-weakly alkaline fluids at temperatures of 150–300 °C (Simpson et al., 2015), suggesting that the fluids responsible for the stibnite precipitation could be alkaline or at least weakly alkaline. This finding is further supported by that an intensive alkaline fluid-rock interaction (reflected by extensive sericitization) was observed enveloping ore veins. Therefore, the pH decreasing during fluid-rock interactions may be an important control of stibnite precipitation. Moreover, as aforementioned, the sulfur in the fluids at Banxi was likely sourced from the dissolution of sulfides (Fig. 4f) in the Proterozoic basement sequences in the Banxi district (BGMRHN, 1988). Thus, we speculate that sulfidation may also be partly responsible for the stibnite precipitation as intensive arsenopyrite of host rock surrounding ore veins.

5.4. Comparison with neighboring giant Sb deposits

In general, fluid characteristics such as redox state, pressure, temperature, and fluid source regions are the main controls on the concentrations of trace elements in ore minerals (Landtwing and Pettke, 2005; Wark and Watson, 2006; Cook et al., 2009; Thomas et al., 2010; Ciobanu et al., 2013; Reich et al., 2013; George et al., 2015; Fu et al., 2020a); therefore, a comparison of the trace element concentrations can be used to reveal the differences in fluid origin and ore-forming processes for various hydrothermal deposits. Compared with the neighboring Woxi and Xikuangshan Sb deposits, stibnite from the Banxi Sb deposit displays a remarkably different trace element composition. For example, stibnite from the Banxi deposit commonly contains measurable Cu and Pb contents, which are comparable to those of the Woxi deposit (varying tens to hundreds of ppm) but are much higher than those of the Xikuangshan deposit that are typically at a level of 0.1–10 ppm (Fu et al., 2020a); moreover, As and Hg contents (Fig. 6a) from the Banxi Sb deposit are generally one or two orders of magnitude lower than those from the Woxi and Xikuangshan Sb deposits (Fu et al., 2020a). The trace element composition of quartz from the Banxi deposit also differs from that of the Woxi and Xikuangshan Sb deposits. For example, the Al concentrations of quartz from the Banxi deposit are much lower than those of the Woxi and Xikuangshan deposits. Generally, Al concentrations in quartz may reflect the ratio of the total Al^{3+} and Si^{4+} activities of the hydrothermal fluid, which was experimentally demonstrated to show a negative correlation with the fluid pH (Rusk et al., 2008). Therefore, lower Al concentrations in quartz are probably indicative of a less acid quartz-participating fluid at Banxi than in the Woxi and Xikuangshan deposits. This difference further suggests that the initial fluids at Banxi were likely alkaline in which Al solubility is relatively lower. In addition, quartz from the Banxi deposit is relatively depleted in alkali metals such as Li, Na, K and Ca (Fig. 6b) than those from the Woxi and Xikuangshan Sb deposits (Fu et al., 2020d and Fig. 7 therein), reflecting the different origins of the quartz-participating fluids. These differences in the trace element composition of stibnite and quartz from different Sb deposits indicate that they were probably generated from fluids with distinct origins. These results further suggest that the Banxi

deposit was generated from basinal brines, differing from the Woxi deposit dominated by metamorphic fluids (Zhu and Peng, 2015) and the Xikuangshan deposit generated mainly by evolved meteoric water (Ma et al., 2003; Hu and Peng, 2018).

5.5. Formation mechanism of the Banxi deposits

The Banxi deposit is generally considered to be a transition between the WX-type and XKS-type Sb deposits, which have some similar characteristics to the former type (e.g., hosted in basement metamorphic rocks) but also show an affinity to the latter type (e.g., characterized by Sb-only mineralization) (Li et al., 2018a; Fu et al., 2019). Considering the geological features and chronological data together with our new data, we invoked a new scenario for the formation of the Banxi Sb deposit: during Early Cretaceous (~130 Ma), the earlier crustal-scale faults were reactivated as a result of the Yanshanian crustal extension (Hu and Zhou, 2012; Mao et al., 2013), which provided favorable conduits for fluid migration. The weakly alkaline initial fluids circulated through these crustal-scale faults such as fault F_1 (a part of the regional Taojiang-Chengbu fault) cutting into the basement sequences, during which leached out a considerable consignment of Sb metals (Li et al., 2019b) as well as sulfurs because of the dissolution of sulfides from underlying and host basement sequences. Subsequently, the decreasing pH of ore-forming fluids coupled with sulfidation during fluid-rock reaction caused Sb metals to precipitate in and/or around fractures, resulting in the formation of stibnite-quartz ore veins within alteration envelopes in the Banxi Sb deposit. This model is distinct from that described for the origin of the WX-type Sb deposits hosted in basement metamorphic rocks but also differs from that of the XKS-type Sb deposits in sedimentary rocks, suggesting that it may have resulted from a unique event, probably related to the Yanshanian crustal extension during the Early Cretaceous.

6. Conclusions

Multiple analyses of individual fluid inclusions, trace element chemistry of cogenetic quartz and stibnite, and He-Ar-S isotopes of hydrothermal sulfides allow a better understanding of the formation mechanism of the Banxi deposit. Individual fluid inclusion analyses suggest that the chemistry of ore-forming fluids at Banxi is distinct from that of magmatic fluids but is comparable to that of basinal fluids. Moreover, remarkable differences in trace element compositions of quartz and stibnite also indicate that the Banxi Sb deposit was probably generated from fluids with a distinct origin. In combination with previous studies and our new data, a new model can be invoked that the weakly alkaline initial fluids dominated by basinal brines circulated through and scavenged Sb and S from the basement metamorphic rocks to form Sb-rich fluids, which then migrated along deep faults and finally precipitated Sb at favorable structural traps (such as fault/fracture zones) resulting in the formation of the world-class Banxi Sb deposit during Early Cretaceous (~130 Ma) under an extensional setting.

Declaration of Competing Interest

The authors declare that they have no known competing financial interests or personal relationships that could have appeared to influence the work reported in this paper.

Acknowledgement

This work was financially supported by the projects of the National Natural Science Foundation of China (41830432, U1812402 and 41703044), the National Key R&D Program of China (2017YFC0602601) and Field Forefront Project of the Key State Laboratary of Ore Deposit Geochemistry, Institute of Geochemistry, Chinese Academy of Sciences (202102). We would like to thank Dr. Zhihui Dai and Dr. Yanwen Tang for their assistance with the LA-ICP-MS analyses at IGGAS.

Appendix A. Supplementary data

Supplementary data to this article can be found online at https://doi.org/10.1016/j.oregeorev.2022.104949.

References

Audétat, A., 2019. The metal content of magmatic-hydrothermal fluids and its relationship to mineralization potential. Economic Geol. Bull. Soc. Econ. Geol. 114: 1033–1056.

Baptiste, P.J., Fouquet, Y., 1996. Abundance and isotopic composition of helium in hydrothermal sulfides from the East Pacific Rise at 13°N. Geochim. Cosmochim. Acta 60, 87–93.

Baker, E.T., Lupton, J.E., 1990. Changes in submarine hydrothermal ^{3}He/heat ratios as an indicator of magmatic/tectonic activity. Nature 346, 556–558.

BGMRHN (Bureau of Geology and Mineral Resources of Hunan Province), 1988. Regional Geology of the Hunan Province. Beijing. Geological Publishing House, 286–507 (in Chinese with English summary).

Burnard, P.G., Hu, R., Turner, G., Bi, X.W., 1999. Mantle, crustal and atmospheric noble gases in Ailaoshan Gold deposits, Yunnan Province, China. Geochim. Cosmochim. Acta 63, 1595–1604.

Burnard, P.G., Polya, D.A., 2004. Importance of mantle-derived fluids during granite associated hydrothermal circulation: He and Ar isotopes of ore minerals from Panasqueira. Geochim. Cosmochim. Acta 68, 1607–1615.

Castro, M.C., Patriarche, D., Goblet, P., 2005. 2-D numerical simulations of groundwater flow, heat transfer and 4He transport – implications for the He terrestrial budget and the mantle helium–heat imbalance. Earth Planet. Sci. Lett. 237, 893–910.

Castro, M.C., Patriarche, D., Goblet, P., Ma, L., Hall, C.M., 2007. ^{4}He/Heat Flux Ratios as New Indicators of Past Thermal and Tectonic Events–New Constraints on the Tectonothermal History of the Michigan Basin. Proceedings of the 4th Mini Conference on Noble Gases in the Hydrosphere and in Natural Gas Reservoirs held at GFZ Potsdam, Germany, 28. 02.-02. 03, 2007.

Charvet, J., Shu, L., Faure, M., Choulet, F., Wang, B.o., Lu, H., Breton, N.L., 2010. Structural development of the Lower Paleozoic belt of South China: genesis of an intracontinental orogen. J. Asian Earth Sci. 39, 309–330.

Chen, L.u., Chen, K., Bao, Z., Liang, P., Sun, T., Yuan, H., 2017. Preparation of standards for in situ sulfur isotope measurement in sulfides using femtosecond laser ablation MC-ICP-MS. J. Anal. At. Spectrom. 32, 107–116.

Chu, Y., Lin, W., Faure, M., Wang, Q., Ji, W., 2012a. Phanerozoic tectonothermal events of the Xuefengshan Belt, central South China: Implications from U-Pb age and Lu-Hf determinations of granites. Lithos 150, 243–255.

Chu, Y., Faure, M., Lin, W., Wang, Q.C., Ji, W.B., 2012b. Tectonics of the Middle Triassic intracontinental Xuefengshan Belt, South China: new insights from structural and chronological constraints on the basal decollement zone. Int. J. Earth Sci. 101, 2125–2150.

Ciobanu, C.L., Cook, N.J., Kelson, C.R., Guerin, R., Kalleske, N., Danyushevsky, L., 2013. Trace element heterogeneity in molybdenite fingerprints stages of mineralization. Chem. Geol. 347, 175–189.

Cook, N.J., Ciobanu, C.L., Pring, A., Skinner, W., Shimizu, M., Danyushevsky, L., Saini-Eidukat, B., Melcher, F., 2009. Trace and minor elements in sphalerite: a LA-ICPMS study. Geochem. Cosmochim. Acta 73, 4761–4791.

Faure, M., Shu, L.S., Wang, B., Charvet, J., Choulet, F., Monié, P., 2009. Intracontinental subduction: a possible mechanism for the Early Paleozoic Orogen of SE China. Terra Nova 21, 360–368.

Fu, S., Hu, R., Bi, X., Chen, Y., Yang, J., Huang, Y., 2015. Origin of Triassic granites in central Hunan Province, South China: constraints from zircon U-Pb ages and Hf and O isotopes. Int. Geol. Rev. 57, 97–111.

Fu, S., Hu, R., Yan, J., Lan, Q., Gao, W., 2019. The mineralization age of the Banxi Sb deposit in Xiangzhong metallogenic province in southern China. Ore Geol. Rev. 112, 103033. https://doi.org/10.1016/j.oregeorev.2019.103033.

Fu, S., Hu, R., Bi, X., Sullivan, N.A., Yan, J., 2020a. Trace element composition of stibnite: Substitution mechanism and implications for the genesis of Sb deposits in southern China. Appl. Geochem. 118, 104637. https://doi.org/10.1016/j.apgeochem.2020.104637.

Fu, S., Hu, R., Batt, G.E., Danišík, M., Evans, N.J., Mi, X., 2020b. Zircon (U-Th)/He thermochronometric constraints on the mineralization of the giant Xikuangshan Sb deposit in central Hunan, South China. Miner. Deposita 55, 901–912.

Fu, S., Hu, R., Yin, R., Yan, J., Mi, X., Song, Z., Sullivan, N.A., 2020c. Mercury and in situ sulfur isotopes as constraints on the metal and sulfur sources for the world's largest Sb deposit at Xikuangshan, Southern China. Miner. Deposita 55, 1353–1364.

Fu, S.L., Lan, Q., Yan, J., 2020d. Trace element chemistry of hydrothermal quartz and its genetic significance: a case study from two giant Sb deposits in southern China. Ore Geol. Rev. 126, 103732.

Fu, S.Y., Shen, C.M., 2020. Geological characteristics of Banxi antimony deposit in Taojiang County of Hunan Province. Geol. Survey China 7, 30–37 (in Chinese with English abstract).

Garofalo, P.S., 2012. The composition of Alpine marine sediments (Bündnerschiefer Formation, W Alps) and the mobility of their chemical components during orogenic metamorphism. Lithos 128-131, 55–72.

George, L., Cook, N.J., Ciobanu, C.L., Wade, B.P., 2015. Trace and minor element in galena: a reconnaissance LA-ICP-MS study. Am. Mineral. 100, 548–569.
Gu, X.X., Zhang, Y.M., Schulz, O., Vavtar, F., Liu, J.M., Zheng, M.H., Zheng, L., 2012. The Woxi W-Sb-Au deposit in Hunan, South China: an example of Late Proterozoic sedimentary exhalative (SEDEX) mineralization. J. Asian Earth Sci. 57, 54–75.
Guillong, M., Latkoczy, C., Seo, J.H., Günther, D., Heinrich, C.A., 2008. Determination of sulfur in fluid inclusions by laser ablation ICP–MS. J. Anal. At. Spectrom. 23, 1581. https://doi.org/10.1039/b807383j.
Halter, W., Pettke, T., Heinrich, C.A., Rothen-Rutishauser, B., 2002. Major to trace element analyses of melt inclusions by laser ablation-ICP-MS: Methods of quantification. Chem. Geol. 183, 63–86.
He, J., Ma, D.S., 1996. Leaching experiment of gold, antimony, mercury and arsenic from the strata under epithermal-mesothermal conditions in sulfur- and chlorine-bearing solutions. Geol. Rev. 42, 76–85 (in Chinese with English abstract).
Heijlen, W., Banks, D.A., Muchez, P., Stensgard, B.M., Yardley, B.W.D., 2008. The nature of mineralizing fluids of the Kipushi Zn-Cu Deposit, Katanga, Democratic Republic of Congo: quantitative fluid inclusion analysis using laser ablation ICP-MS and Bulk Crush-Leach Methods. Econ. Geol. 103, 1459–1482.
Heinrich, C.A., Günther, D., Audétat, A., Ulrich, T., Frischknecht, R., 1999. Metal fractionation between magmatic brine and vapor, determined by microanalysis of fluid inclusions. Geology 27, 755–758.
Heinrich, C.A., Pettke, T., Halter, W.E., Aigner-Torres, M., Audétat, A., Günther, D., Hattendorf, B., Bleiner, D., Guillong, M., Horn, I., 2003. Quantitative multi-element analysis of minerals, fluid and melt inclusions by laser-ablation inductively-coupled-plasma mass- spectrometry. Geochim. Cosmochim. Acta 67, 3473–3497.
Hoefs, J., 2015. Stable Isotope Geochemistry, 7th edition. Springer International Publishing, Switzerland, p. 97.
Hu, A.X., Peng, J.T., 2018. Fluid inclusions and ore precipitation mechanism in the giant Xikuangshan mesothermal antimony deposit, South China: conventional and infrared microthermometric constraints. Ore Geol. Rev. 95, 49–64.
Hu, R.Z., 2021. Large Scale Low-temperature Metallogenesis in South China. Science Press, Beijing, pp. 219–269 (in Chinese).
Hu, R.Z., Bi, X.W., Turner, G., Burnard, P.G., 1999. He and Ar isotopic geochemistry of the ore-forming fluids of the Ailaoshan Au ore belt. Sci. China (Series D) 29, 321–330.
Hu, R.Z., Burnard, P.G., Bi, X.W., Zhou, M.F., Pen, J.T., Su, W.C., Wu, K.X., 2004. Helium and argon isotope geochemistry of alkaline intrusion-associated gold and copper deposits along the Red River-Jinshajiang fault belt, SW China. Chem. Geol. 203, 305–317.
Hu, R.Z., Burnard, P.G., Bi, X.W., Zhou, M.F., Peng, J.T., Su, W.C., Zhao, J.H., 2009. Mantle- derived gaseous components in ore-forming fluids of the Xiangshan uranium deposit, Jiangxi province, China: evidence from He, Ar and C isotopes. Chem. Geol. 266, 86–95.
Hu, R.Z., Bi, X.W., Jiang, G.H., Chen, H.W., Peng, J.T., Qi, Y.Q., Wu, L.Y., Wei, W.F., 2012. Mantle–derived noble gases in ore–forming fluids of the granite-related Yaogangxian tungsten deposit, Southeastern China. Miner. Deposita 47, 623–632.
Hu, R.Z., Fu, S.L., Xiao, J.F., 2016. Major scientific problems on low–temperature metallogenesis in South China. Acta Petrologica Sinica 32, 3239–3251 (in Chinese with English abstract).
Hu, R., Fu, S., Huang, Y., Zhou, M.F., Fu, S., Zhao, C., Wang, Y., Bi, X., Xiao, J., 2017. The giant South China Mesozoic low-temperature metallogenic domain: reviews and a new geodynamic model. J. Asian Earth Sci. 137, 9–34.
Hu, R.Z., Zhou, M.F., 2012. Multiple Mesozoic mineralization events in South China–an introduction to the thematic issue. Miner. Deposita 47, 579–588.
Hu, X.W., Pei, R.F., Zhou, S., 1996. Sm-Nd dating for antimony mineralization in the Xikuangshan deposit, Hunan, China. Resour. Geol. 46, 227–231.
Jiang, Z.Y., Wei, L.M., Chen, M.Y., 1990. Sulfur isotopic study of sulfides from sedimentary strata and strata-bound deposits in Hunan, Guangdong and Guangxi of Southern China. Geochemica 19, 117–126 (In Chinese with English abstract).
Kendrick, M.A., Burnard, P.G., 2013. Noble gases and halogens in fluid inclusions: A journey through the Earth's crust. In: Burnard, P.G. (Ed.), The noble gases as geochemical tracers. Springer, Heidelberg, pp. 319–369.
Kharaka, Y.K., Hanor, J.S., 2014. Deep fluids in sedimentary basins. In: Holland, H., Turekian, H.D.H.K. (Eds.), Treatise on Geochemistry (second edition). Elsevier, Oxford, UK, pp. 471–515.
Klemm, L.M., Pettke, T., Heinrich, C.A., 2008. Fluid and source magma evolution of the Questa porphyry Mo deposit, New Mexico, USA. Miner. Deposita 43, 533–552.
Korges, M., Weis, P., Lüders, V., Laurent, O., 2018. Depressurization and boiling of a single magmatic fluid as a mechanism for tin-tungsten deposit formation. Geology 46, 75–78.
Krupp, R.E., 1988. Solubility of stibnite in hydrogen sulfide solutions, speciation, and equilibrium constants, from 25 to 350 °C. Geochim. Cosmochim. Acta 52, 3005–3015.
Lan, T.G., Hu, R.Z., Bi, X.W., Mao, G.J., Wen, B.J., Liu, L., Chen, Y.H., 2018. Metasomatized asthenospheric mantle contributing to the generation of Cu-Mo deposits within an intracontinental setting: a case study of the ~128 Ma Wangjiazhuang Cu-Mo deposit, eastern North China Craton. Journal of Asian Earth Science 160, 460–489.
Landtwing, M.R., Pettke, T., 2005. Relationships between SEM-cathodoluminescence response and trace-element composition of hydrothermal vein quartz. Am. Mineral. 90, 122–131.
Large, S.J.E., Bakker, E.Y.N., Weis, P., Wälle, M., Ressel, M., Heinrich, C.A., 2016. Trace elements in fluid inclusions of sediment–hosted gold deposits indicate a magmatic hydrothermal origin of the Carlin ore trend. Geology 44, 1015–1018.
Li, J.H., Zhang, Y.Q., Xian, X.B., Li, H.L., Dong, S.W., Li, T.D., 2014. SHRIMP U-Pb dating of zircons from the Baimashan Longtan super-unit and Wawutang granites in Hunan Province and its geological implication. J. Jilin Univ.: Earth Sci. Ed. 44, 158–175.
Li, H., Wu, Q.H., Evans, N.J., Zhou, Z.K., Kong, H., Xi, X.S., Lin, Z.W., 2018a. Geochemistry and geochronology of the Banxi Sb deposit: Implications for fluid origin and the evolution of Sb mineralization in central-western Hunan, South China. Gondwana Res. 55, 112–134.
Li, H., Kong, H., Zhou, Z.K., Tindell, T., Tang, Y.Q., Wu, Q.H., Xi, X.S., 2019a. Genesis of the Banxi Sb deposit, South China: constraints from wall-rock geochemistry, fluid inclusion microthermometry, Rb-Sr geochronology, and H-O-S isotopes. Ore Geol. Rev. 115, 103162.
Li, H., Zhou, Z.K., Evans, N.J., Kong, H., Wu, Q.H., Xi, X.S., 2019b. Fluid-zircon interaction during low-temperature hydrothermal processes: Implications for the genesis of the Banxi antimony deposit, South China. Ore Geol. Rev. 114, 103137. https://doi.org/10.1016/j.oregeorev.2019.103137.
Li, H., Danišík, M., Zhou, Z.K., Jiang, W.C., Wu, J.H., 2020. Integrated U-Pb, Lu-Hf and (U-Th)/He analysis of zircon from the Banxi Sb deposit and its implications for the low-temperature mineralization in South China. Geosci. Front. 11, 1323–1335.
Li, H.T., Cao, D.Y., Wang, L.J., Guo, A.J., Li, Y.F., Xu, H., 2013. Characteristics and evolution of coal–controlled structures on the east slope of the Xuefengshan domain in central Hunan Province. Geotectonica et Metallogenia 37, 611–621 (in Chinese with English abstract).
Li, S.S., 1996. Evolution of antimony mineralization by the mantle plume of deep fluid in central Hunan. Hunan Geol. 15,137–142 (in Chinese with English abstract).
Li, W., Xie, G.Q., Mao, J.W., Zhang, Z.Y., Fu, B., Lu, S., 2018b. Muscovite 40Ar/39Ar and in situ sulfur isotope analyses of the slate-hosted Gutaishan Au-Sb deposit, South China: implications for possible Late Triassic magmatic-hydrothermal mineralization. Ore Geol. Rev. 101, 839–853.
Li, Z.X., Li, X.H., Wartho, J.A., Clark, C., Li, W.X., Zhang, C.L., Bao, C., 2010. Magmatic and metamorphic events during the early Paleozoic Wuyi-Yunkai orogeny, southeastern South China: new age constraints and pressure-temperature conditions. Geol. Soc. Am. Bull. 122, 772–793.
Liu, Y., Hu, Z., Gao, S., Günther, D., Xu, J., Gao, C., Chen, H., 2008. In situ analysis of major and trace elements of anhydrous minerals by LA-ICP-MS without applying an internal standard. Chem. Geol. 257, 34–43.
Lu, H.Z., Fan, H.R., Ni, P., Ou, G.X., Shen, K., Zhang, W.Z., 2004. Fluid Inclusions. Science Press, Beijing, pp. 205–209 (in Chinese).
Lu, X.W., Ma, D.S., Xie, Q.L., Wang, W.Y., 2001. Trace element geochemical characteristics of Neoproterozoic-Paleozoic strata in western and central Hunan. Geol.-Geochem. 29, 24–30 (in Chinese with English abstract).
Luo, X.L., 1995. Geological characteristics of the formation of Banxi antimony deposits in Hunan. J. Guilin Inst. Technol. 15, 231–242 (in Chinese with English abstract).
Lupton, J.E., Baker, E.T., Massoth, G.J., 1989. Variable 3He/heat ratios in submarine hydrothermal systems: evidence from two plumes over the Juan de Fuca ridge. Nature 337, 161–164.
Ma, D.S., Pan, J.Y., Xie, Q.L., He, J., 2002. Ore source of Sb (Au) deposits in Center Hunan: I. Evidences of trace elements and experimental geochemistry. Mineral Deposits 3, 366–376 (in Chinese with English abstract).
Ma, D.S., Pan, J.Y., Xie, Q.L., 2003. Ore sources of Sb (Au) deposits in Center Hunan: II. Evidence of isotopic geochemistry. Mineral Deposits 21, 78–87 (in Chinese with English abstract).
Mao, J.W., Cheng, Y.B., Chen, M.H., Pirajno, F., 2013. Major types and time-space distribution of Mesozoic ore deposits in South China and their geodynamic settings. Miner. Deposita 48, 267–294.
Mark, D.F., Stuart, F.M., de Podesta, M., 2011. New high-precision measurements of the isotopic composition of atmospheric argon. Geochim. Cosmochim. Acta 75, 7494–7501.
Niu, H.C., Ma, D.S., 1991. Experimental geochemistry of gold, antimony and tungsten during water-rock interactions under low-temperature, open system. Chin. Sci. Bull. 36, 1879–1881 (in Chinese with English abstract).
Obolensky, A.A., Gushchina, L.V., Borisenko, A.S., Borovikov, A.A., Pavlova, G.G., 2007. Antimony in hydrothermal processes: solubility, conditions of transfer, and metal-bearing capacity of solutions. Russian Geol. Geophys. 48, 992–1001.
Oelkers, E.H., Sherman, D.M., Ragnarsdottir, K.V., Collins, C., 1998. An EXAFS spectroscopic study of aqueous antimony(III)-chloride complexation at temperatures from 25 to 250°C. Chem. Geol. 151, 21–27.
Ohmoto, H., Rye, R.O., 1979. Isotopes of sulfur and carbon. In: Barnes, H.L. (Ed.), Geochemistry of Hydrothermal Ore Deposits. Wiley, New York, pp. 509–567.
Ohmoto, H., 1986. Stable isotopes in high temperature geological process. Rev. Mineral. Geochem. 16, 491–559.
Pan, J.Y., Ni, P., Wang, R.C., 2019. Comparison of fluid processes in coexisting wolframite and quartz from a giant vein-type tungsten deposit, South China: insights from detailed petrography and LA-ICP-MS analysis of fluid inclusions. Am. Mineral. 104, 1092–1116.
Peng, J.T., Hu, R.Z., Jiang, G.H., 2003a. Samarium-neodymium isotope system of fluorites from the Qinglong antimony deposit, Guizhou Province: constraints on the mineralizing age and ore-forming minerals sources. Acta Petrologica Sinica 19, 785–791 (in Chinese with English abstract).
Peng, J.T., Hu, R.Z., Burnard, P.G., 2003b. Samarium-neodymium isotope systematics of hydrothermal calcite from the Xikuangshan antimony deposit (Hunan, China): the potential of calcite as a geochronometer. Chem. Geol. 200, 129–136.
Phillips, G.N., Powell, R., 2010. Formation of gold deposits: a metamorphic devolatilization model. J. Metamorphic Geol. 28, 689–718.
Pitcairn, I.K., Teagle, D.A.H., Craw, D., Olivo, G.R., Kerrich, R., Brewer, T.S., 2006. Sources of metals and fluids in orogenic gold deposits: insights from the Otago and Alpine Schists, New Zealand. Econ. Geol. 101, 1525–1546.

Pitcairn, I.K., Skelton, A.D.L., Wohlgemuth-Ueberwasser, C.C., 2015. Mobility of gold during metamorphism of the Dalradian in Scotland. Lithos 233, 69–88.
Pokrovski, G.S., Zakirov, I.V., Roux, J., Testemale, D., Hazemann, J.L., Bychkov, A.Y.u., Golikova, G.V., 2002. Experimental study of arsenic speciation in vapor phase to 500°C: implications for As transport and fractionation in low-density crustal fluids and volcanic gases. Geochim. Cosmochim. Acta 66, 3453–3480.
Pokrovski, G.S., Borisova, A.Y., Roux, J., Hazemann, J.L., Petdang, A., Tella, M., Testemale, D., 2006. Antimony speciation in saline hydrothermal fluids: a combined X-ray absorption fine structure spectroscopy and solubility study. Geochim. Cosmochim. Acta 70, 4196–4214.
Qiu, L., Yan, D.P., Tang, S.L., Wang, Q., Yang, W.X., Tang, X., Wang, J., 2016. Mesozoic geology of southwestern China: Indosinian foreland overthrusting and subsequent deformation. J. Asian Earth Sci. 122, 91–105.
Rao, J.R., Luo, J.L., Yi, Z.J., 1999. The mantle-crustal tectonic metallogenic model and ore- prospecting prognosis in the Xikuangshan antimony ore field. Geophys. Geochem. Explor. 23, 241–249 (In Chinese with English abstract).
Reich, M., Deditius, A., Chryssoulis, S., Li, J.W., Ma, C.Q., Parada, M.A., Barra, F., Mittermayr, F., 2013. Pyrite as a record of hydrothermal fluid evolution in a porphyry copper system: a SIMS/ EMPA trace element study. Geochim. Cosmochim. Acta 104, 42–62.
Rusk, B.G., Lowers, H.A., Reed, M.H., 2008. Trace elements in hydrothermal quartz: relationships to cathodoluminescence textures and insights into vein formation. Geology 36, 547–550.
Rusk, B.G., Reed, M.H., Dilles, J.H., Klemm, L.M., Heinrich, C.A., 2004. Compositions of magmatic hydrothermal fluids determined by LA-ICP-MS of fluid inclusions from the porphyry copper–molybdenum deposit at Butte, MT. Chem. Geol. 210, 173–199.
Samson, I.M., Williams-Jones, A.E., Ault, K.M., Gagnon, J.E., Fryer, B.J., 2008. Source of fluids forming distal Zn-Pb-Ag skarns: Evidence from laser ablation–inductively coupled plasma–mass spectrometry analysis of fluid inclusions from El Mochito, Honduras. Geology 36, 947. https://doi.org/10.1130/G25214A.1.
Seal, R.R., 2006. Sulfur isotope geochemistry of sulfide minerals. Rev. Mineral. Geochem. 61, 633–677.
Shi, M.K., Fu, B.Q., Jin, X.X., 1993. Antimony metallogeny in central part of Hunan Province. Changsha: Hunan Press of Science and Technology, 1–151 (in Chinese).
Shu, Q., Chang, Z., Hammerli, J., Lai, Y., Huizenga, J.M., 2017. Composition and evolution of fluids forming the Baiyinnuo'er Zn-Pb skarn deposit, northeastern china: insights from laser ablation ICP-MS study of fluid inclusions. Econ. Geol. 112, 1441–1460.
Shu, Q., Chang, Z., Mavrogenes, J., 2021. Fluid compositions reveal fluid nature, metal deposition mechanisms, and mineralization potential: An example at the Haobugao Zn-Pb skarn, China. Geology 49, 473–477.
Simpson, M.P., Palinkas, S.S., Mauk, J.L., Bodnar, R.J., 2015. Fluid inclusion chemistry of adularia- sericite epithermal Au-Ag deposits of the southern Hauraki Goldfield, New Zealand. Econ. Geol. 110, 763–786.
Stuart, F.M., Turner, G., Duckworth, R.C., Fallick, A.E., 1994. Helium isotopes as tracers of trapped hydrothermal fluids in ocean-floor sulfides. Geology 22, 823–826.
Stuart, F.M., Burnard, P.G., Taylor, R.P., Turner, G., 1995. Resolving mantle and crustal contributions to ancient hydrothermal fluids: He-Ar isotopes in fluid inclusions from DaeHwa W-Mo mineralisation, South Korea. Geochim. Cosmochim. Acta 59, 4663–4673.
Spycher, N., Reed, M.H., 1989. Evolution of a Broadlands-type epithermal fluid along alternative P-T path: implications for the transport and deposition of base, precious and volatile metals. Econ. Geol. 84, 328–359.
Tang, Y.Q., Kong, H., Wu, Q.H., Xi, X.S., 2017. Study on fluid inclusions of the Banxi antimony deposit. Contrib. Geol. Min. Resour. Res. 32, 391–396.
Thomas, J.B., Bruce Watson, E., Spear, F.S., Shemella, P.T., Nayak, S.K., Lanzirotti, A., 2010. TitaniQ under pressure: the effect of pressure and temperature on the solubility of Ti in quartz. Contrib. Mineral. Petrol. 160, 743–759.
Turner, G., Burnard, P.G., Ford, J.L., Gilmour, J.D., Lyon, I.C., Stuart, F.M., 1993. Tracing fluid sources and interaction. Philos. Trans. R. Soc. Lond. 344, 127–140.
Wan, Y., Liu, D., Wilde, S.A., Cao, J., Chen, B., Dong, C., Song, B., Du, L., 2010. Evolution of the Yunkai Terrane, South China: Evidence from SHRIMP zircon U-Pb dating, geochemistry and Nd isotope. J. Asian Earth Sci. 37, 140–153.
Wang, C., Shao, Y.J., Evans, N.J., Li, H., Zhou, H.d., Huang, K.X., Liu, Z.f., Chen, Y., Lai, C., Liu, Q.Q., 2020. Genesis of Zixi gold deposit in Xuefengshan, Jiangnan Orogen (South China): age, geology and isotopic constraints. Ore Geol. Rev. 117, 103301. https://doi.org/10.1016/j.oregeorev.2019.103301.
Wang, K.X., Chen, P.R., Chen, W.F., Ling, H.F., Zhao, K.D., Yu, Z.Q., 2012a. Magma mingling and chemical diffusion in the Taojiang granitoids in the Hunan Province, China: evidences from petrography, geochronology and geochemistry. Mineral. Petrol. 106, 243–264.
Wang, Y., Fan, W., Sun, M., Liang, X., Zhang, Y., Peng, T., 2007. Geochronological, geochemical and geothermal constraints on petrogenesis of the Indosinian peraluminous granites in the South China Block: a case study in the Hunan Province. Lithos 96, 475–502.
Wang, Y.L., Chen, Y.C., Wang, D.H., Xu, J., Chen, Z.H., 2012b. Scheelite Sm-Nd dating of the Zhazixi W-Sb deposit in Hunan and its geological significance. Geol. China 39, 1339–1344.
Wark, D.A., Watson, E.B., 2006. TitaniQ: A titanium-in-quartz geothermometer. Contrib. Mineral. Petrol. 152, 743–754.
Wei, W.F., Hu, R.Z., Bi, X.W., Jiang, G.H., Yan, B., Yin, R.S., Yang, J.H., 2019. Mantle-derived and crustal He and Ar in the ore-forming fluids of the Xihuashan granite-associated tungsten ore deposit, South China. Ore Geol. Rev. 105, 605–615.
Williams-Jones, A.E., Normand, C., 1997. Controls of mineral parageneses in the system of Fe- Sb-S-O. Econ. Geol. 92, 308–324.
Williams-Jones, A.E., Samson, I.M., Ault, K.M., Gagnon, J.E., Fryer, B.J., 2010. The genesis of distal zinc skarns: evidence from the Mochito deposit, Honduras. Econ. Geol. 105, 1411–1440.
Wilson, S.A., Ridley, W.I., Koenig, A.E., 2002. Development of sulfide calibration standards for the laser ablation inductively-coupled plasma mass spectrometry technique. J. Anal. At. Spectrom. 17, 406–409.
Wood, S.A., Crerar, D.A., Borcsik, M.P., 1987. Solubility of the assemblage pyrite-pyrrhotite-magnetite-sphalerite-galena-gold-stibnite-bismuthinite-argentite-molybdenite in H_2O-NaCl- CO2 solutions from 200 to 350°C. Econ. Geol. 82, 1864–1887.
Wu, L.Y., Hu, R.Z., Peng, J.T., Bi, X.W., Jiang, G.H., Chen, H.W., Wang, Q.Y., Liu, Y.Y., 2011. He and Ar isotopic compositions and genetic implications for the giant Shizhuyuan W-Sn-Bi-Mo deposit, Hunan Province, South China. Int. Geol. Rev. 53, 677–690.
Wu, L.Y., Hu, R.Z., Li, X.F., Stuart, F.M., Jiang, G.H., Qi, Y.Q., Zhu, J.J., 2018. Mantle volatiles and heat contributions in high sulfidation epithermal deposit from the Zijinshan Cu-Au-Mo-Ag orefield, Fujian Province, China: evidence from He and Ar isotopes. Chem. Geol. 480, 58–65.
Wu, X.M., Chen, X.X., 2004. Ore-controlling factor of Banxi stibium mine. Geol. Min. Resour. South China 3, 26–30 (in Chinese with English abstract).
Xie, G., Mao, J., Li, W., Fu, B., Zhang, Z., 2019. Granite-related Yangjiashan tungsten deposit, southern China. Miner. Deposita 54, 67–80.
Yao, J., Shu, L., Cawood, P.A., Li, J., 2016. Delineating and characterizing the boundary of the Cathaysia Block and the Jiangnan orogenic belt in South China. Precambr. Res. 275, 265–277.
Yin, Y., Zajacz, Z., 2018. The solubility of silver in magmatic fluids: Implications for silver transfer to the magmatic hydrothermal ore–forming environment. Geochim. Cosmochim. Acta 238, 235–251.
Yuan, H., Liu, X., Chen, L., Bao, Z., Chen, K., Zong, C., Li, X.C., Qiu, J.W., 2018. Simultaneous measurement of sulfur and lead isotopes in sulfides using nanosecond laser ablation coupled with two multi-collector inductively coupled plasma mass spectrometers. J. Asian Earth Sci. 154, 386–396.
Zhai, D., Mathur, R., Liu, S.A., Liu, J., Godfrey, L., Wang, K., Xu, J., Vervoort, J., 2021. Antimony isotope fractionation in hydrothermal systems. Geochim. Cosmochim. Acta 306, 84–97.
Zhang, Z., Xie, G., Mao, J., Liu, W., Olin, P., Li, W., 2019. Sm-Nd dating and in-situ LA–ICP–MS trace element analyses of Scheelite from the Longshan Sb-Au Deposit, Xiangzhong Metallogenic Province, South China. Minerals 9, 87. https://doi.org/10.3390/min9020087.
Zhao, J.H., Peng, J.T., Hu, R.Z., Fu, Y.Z., 2005. Chronology, petrology, geochemistry and tectonic environment of Banxi quartz porphyry dikes, Hunan Province. Acta Geoscientica Sinica 26, 525–534 (in Chinese with English abstract).
Zhao, J.H., Zhou, M.F., Yan, D.P., Zheng, J.P., Li, J.W., 2011. Reappraisal of the ages of Neoproterozoic strata in South China: no connection with the Grenvillian orogeny. Geology 39, 299–302.
Zhu, J.W., Chen, Q.C., Wang, G.D., 2002. Metallogeny and prospecting model of antimony deposits at the northeastern section of the Taojiang-Chengbu fault zone in Hunan. Geol. Rev. 48, 89–95 (in Chinese with English abstract).
Zhu, Y.N., Peng, J.T., 2015. Infrared microthermometric and noble gas isotope study of fluid inclusions in ore minerals at the Woxi orogenic Au–Sb–W deposit, western Hunan, South China. Ore Geol. Rev. 65, 55–69.
Zotov, A.V., Shikina, N.D., Akinfiev, N.N., 2003. Thermodynamic properties of the Sb (III) hydroxide complex Sb (OH)3(aq) at hydrothermal conditions. Geochim. Cosmochim. Acta 67, 1821–1836.
Zou, H., Li, M., Bagas, L., Li, Y., Fang, Y., Cao, H.W., Jiang, X.W., Chen, H.F., 2020. Fluid composition and evolution of the Langxi Ba-F deposit, Yangtze Block, China: new insight from LA-ICP-MS study of individual fluid inclusion. Ore Geol. Rev. 125, 103702.